William Scott Grundeland Olsen

Spatial Non-Stationary Bayesian Analysis of Deterioration of Pavement With Uncertainty

A Case Study of the European Route E16 Between Bergen and Voss in Western Norway

Master's thesis in Applied Physics and Mathematics
Supervisor: Ingelin Steinsland
June 2022

Master's thesis

NTNU
Norwegian University of Science and Technology
Faculty of Information Technology and Electrical Engineering
Department of Mathematical Sciences

NTNU
Norwegian University of
Science and Technology

William Scott Grundeland Olsen

Spatial Non-Stationary Bayesian Analysis of Deterioration of Pavement With Uncertainty

A Case Study of the European Route E16 Between Bergen and Voss in Western Norway

Master’s thesis in Applied Physics and Mathematics
Supervisor: Ingelin Steinsland
June 2022

Norwegian University of Science and Technology
Faculty of Information Technology and Electrical Engineering
Department of Mathematical Sciences

NTNU
Norwegian University of
Science and Technology

Spatial Non-Stationary Bayesian Analysis of Deterioration of Pavement With Uncertainty

A Case Study of the European Route E16 Between Bergen and Voss in Western Norway

William Scott Grundeland Olsen
Master's Thesis, Spring 2022

NTNU
Faculty of Information Technology
and Electrical Engineering
Department of Mathematical Sciences

Statens vegvesen
Norwegian Public Roads
Administration

This master's thesis is submitted under the master's program *Applied Physics and Mathematics*, with program option *Industrial Mathematics*, at the Department of Mathematical Sciences, Norwegian University of Science and Technology (NTNU). The scope of the report is 30 credits, and fulfils TMA4900 – Industrial Mathematics, Master's Thesis.

Abstract

A well maintained pavement is important for road safety, and targeted maintenance is important for maximising the socioeconomic impact from the resources allocated. Through the project SMARTer maintenance, the Norwegian University of Science and Technology (NTNU) and the Norwegian Public Roads Administration target this problem by developing technology, methods and competence to improve and streamline maintenance of Norway's road network.

This thesis investigates the change in rut depth, the rutting, as a measure of pavement deterioration, along the European route E16 between Bergen and Voss in the Western part of Norway for the years 2015 to 2020. The aim is to locate factors responsible for increased rutting, and use the results to predict the rut depth forward in time. We investigate the effect of traffic intensity, road width, and road cover type, being either asphalt concrete (Ab), asphalt gravel concrete (Agb), or stone mastic asphalt (Ska). We also investigate adding spatial fields to the model, and include a random yearly effect. A spatial stationary model, and a spatial non-stationary model varying with the traffic intensity are presented. The spatial fields consist of one time constant common field, and annually varying spatial fields. The models are proposed within a Bayesian framework as latent Gaussian models (LGMs), where the spatial fields are modeled as Gaussian random fields (GRFs).

The results show that there are evidence that there is a spatial dependence, and that that spatial dependence varies with the traffic intensity. The spatial non-stationary model is therefore used for prediction. The results show that road cover type stone mastic asphalt gives the least expected rutting, while road cover type asphalt gravel concrete gives the most. The expected rutting also increases with an increase in traffic intensity. When the road width is narrower, the expected rutting increases, following from the fact that when the road is narrow, the wheels of the vehicles lie in the same lane leading to more stress on the road at this point. The spatial effect from the time constant common field gives the difference from the expected rutting if there were no spatial effect. This shows that there is less than expected rutting near Bergen, and more than expected rutting towards Voss. Prediction of the rutting for the European route E16 between Bergen and Voss is done for the year 2021, allowing to calculate the predicted rut depth. Based on limits of the rut depth before repaving, a stretch exceeding this is identified.

Sammendrag

Et godt vedlikeholdt vegdekke er viktig for trafikksikkerheten og målrettet vedlikehold er viktig for å maksimere den samfunnsøkonomiske effekten av ressursene som tildeles. Gjennom prosjektet SMARTere vedlikehold har Norges teknisk-naturvitenskapelige universitet (NTNU) og Statens vegvesen angrepet denne problemstillingen ved å utvikle teknologi, metoder og kompetanse for å forbedre og effektivisere vedlikeholdet av det norske vegnett.

Denne avhandlingen undersøker endringen i spordybde som mål på vegdekkeslitasje langs Europavei 16 (E16) mellom Bergen og Voss på Vestlandet for årene 2015 til 2020. Målet er å lokalisere faktorer som er ansvarlige for økt spordannelse, og å bruke resultatene til å forutsi spordybden frem i tid. Vi undersøker effekten av trafikkintensitet, vegbredde, og vegdekketype, bestående enten av asfaltbetong (Ab), asfaltgrusbetong (Agb) eller skjelletasfalt (Ska). Vi undersøker også å legge til romlige felt i modellen og inkluderer en tilfeldig årseffekt. En romlig stasjonær modell og en romlig ikke-stasjonær modell som varierer med trafikkintensiteten presenteres. De romlige feltene består av ett tidskonstant felles felt, og årlig varierende romlige felt. Modellene er foreslått innenfor et Bayesiansk rammeverk som latente Gaussiske modeller (LGM), hvor de romlige feltene er modellert som Gaussiske tilfeldige felt (GRF).

Resultatene viser at det er tegn for at det er en romlig avhengighet, og at den romlige avhengigheten varierer med trafikkintensiteten. Den romlige ikke-stasjonære modellen brukes derfor til prediksjon. Resultatene viser at vegdekketypen skjelettasfalt gir minst forventet spordannelse, mens vegdekketypen asfaltgrusbetong gir mest. Forventet spordannelse øker også med økt trafikkintensitet. Når vegbredden er smalere, øker den forventede spordannelsen, som følger av at når vegen er smal ligger hjulene på kjøretøyene i tilnærmet samme posisjon hele tiden, som fører til mer belastning på denne delen av vegen. Den romlige effekten fra det tidskonstante felles feltet gir forskjellen fra forventet spordannelse dersom det ikke var inkludert en romlig effekt. Dette visert at det er ventet mindre enn antatt spordannelse nær Bergen, og at det er ventet mer enn antatt spordannelse mot Voss. Prediksjon av spordannelse for E16 mellom Bergen og Voss gjøres for år 2021, som gjør det mulig å beregne forventet spordybde. Basert på grenser spordybden kan bli før asfaltering må skje, identifiserer en strekning som overskrider denne og trenger asfaltering.

Acknowledgements

I would like to thank my supervisor, professor Ingelin Steinsland for useful discussions, feedback, guidance, and helping words along the way in my work. Thanks are also given to Natoya O.A.S. Jourdain for helpful discussions and talks along the way, and to Emil Vedvik for allowing me to further expand on his work, and for passing on relevant data and code. For their help explaining the different types of data and helping otherwise, I would also like to thank Dagfin Gryteselv and Siebert Doreen at the Norwegian Public Road Administration.

Finally, I would like to thank my friends and family for their support and encouragement along the way.

William Scott Grundeland Olsen
Trondheim, June 2022

Contents

Abstract **i**

Sammendrag **ii**

Acknowledgements **iii**

Contents **iv**

List of Figures **vi**

List of Tables **viii**

1 Introduction **1**

2 Study Area, Data, and Exploratory Data Analysis **5**
2.1 European Route E16 Between Bergen and Voss 5
2.2 Rutting 6
2.2.1 Data 6
2.2.2 Cleaning of Data 7
2.3 Traffic Intensity 9
2.4 Road Cover Type 11
2.5 Road Width 11
2.6 Exploratory Data Analysis 12

3 Background **16**
3.1 Bayesian Inference 16
3.2 Latent Gaussian Models 17
3.3 Gaussian Random Fields 18
3.3.1 Gaussian Markov Random Fields 18
3.4 The Laplace Approximation 18
3.5 Integrated Nested Laplace Approximations 19
3.6 The Stochastic Partial Differential Equation Approach to Spatial Modeling 20
3.6.1 Stationarity 20
3.6.2 Non-Stationarity 21
3.7 Model Assessment 22

4 Statistical Models and Methods for Rutting 24
4.1 The Latent Gaussian Models for Rutting 24
4.2 The Model Without Spatial Effects 25
4.3 Spatial Stationary Model for Rutting 25
4.3.1 Choosing Priors 26
4.4 Spatial Non-Stationary Model for Rutting 27
4.4.1 Choosing Priors 27
4.5 Inference, Prediction, and the Software 28

5 Results for the Rutting 29
5.1 Fixed Effects, Random Yearly Effect, and Residuals 29
5.1.1 Spatial Non-Stationary Model for Rutting 29
5.1.2 Comparing With Non-Spatial and Spatial Stationary Model for Rutting 32
5.2 Spatial Effects 35
5.2.1 Spatial Non-Stationary Model for Rutting 35
5.2.2 Comparing With Spatial Stationary Model for Rutting 36
5.3 Comparison of the Models 39
5.4 Prediction With Uncertainty 41

6 Discussion, Final Remarks, and Further Work 45

Appendices 47

A Approximation of the Posterior Marginals in INLA 48
A.1 Approximation of the Posterior Marginals for the Hyperparameters 48
A.2 Approximation of the Posterior Marginals for the Latent Field 49

B Estimates of the Parameters for the Spatial Effects 50

C Sum-to-Zero Constraints on the Spatial Fields 52

Bibliography 56

List of Figures

2.1 The study area, enclosed in the green box, is located in the western part of Norway, in Vestland county. 5
2.2 An illustration of the road on the European route E16 between Bergen and Voss. The road lies close to the fjord, and in mountainous terrain. (Photo: Øystein H. Brekke. Published: Wikimedia Commons.) 6
2.3 The density of the rutting for each of the years from 2017 to 2020. 7
2.4 The average annual rutting for each road segment, and the density of the average rutting, over the years 2017 to 2020. 8
2.5 The Euclidean distance between the road segments in 2020 to those in 2015 to 2019. 8
2.6 The rut depth and rutting over the years 2017 to 2020 for a subset of the road containing 250 road segments in a high traffic intensity area in proximity to Ytre Arna in Bergen municipality. 10
2.7 The AADT along the study area. 10
2.8 The mean daily traffic intensity. 11
2.9 The three road covers in the study area, asphalt concrete (Ab), asphalt gravel concrete (Agb), and stone mastic asphalt (Ska). . . 12
2.10 The road width along the road from Bergen to Voss. 13
2.11 The rutting over all the years for some intervals of the AADT. . . 13
2.12 The number of road segments with different values of the AADT for each of the road cover types. 14
2.13 The variogram of the annual semivariance for rutting in the years 2017 to 2020. 15

5.1 The fixed effect of the road cover type and the road width for the spatial non-stationary model for the rutting as a function of the AADT. 30
5.2 The total expected rutting from the fixed effects for each road cover type as a function of the AADT, assuming a road width of 5 meters, for the spatial non-stationary model for the rutting. 30
5.3 The posterior marginal distribution for the standard deviation of the random yearly effect and the residuals for the spatial non-stationary model for the rutting. 31

5.4 The fixed effect of the road cover type and the road width for the spatial non-stationary model in drawn lines, for the spatial stationary model in dashed lines, and for the non-spatial model in dotted lines, all as a function of the AADT. 32
5.5 The total expected rutting from the fixed effects for each road cover type as a function of the AADT, assuming a road width of 5 meters for the spatial non-stationary model in drawn lines, the spatial stationary model in dashed lines, and the non-spatial model in dotted lines. 33
5.6 The posterior marginal distribution for the standard deviation of the random yearly effect and the residuals for the non-spatial model, the spatial stationary model, and the spatial non-stationary model for the rutting. 35
5.7 The rutting inferred from the common spatial field $\omega_{\mathrm{NS}}(s)$ for the non-stationary model with a 95% credible interval and on the map between Bergen and Voss. 36
5.8 The annual spatial deviation from the spatial field $\omega_{\mathrm{NS}}(s)$ for each of the years from 2017 to 2020. 37
5.9 The spatial range and marginal standard deviation for the spatial fields from the spatial non-stationary model as a function of the AADT. 38
5.10 The posterior mean of the rutting from the common spatial field $\omega_{\mathrm{S}}(s)$ for the spatial stationary model with a 95% credible interval and on the map between Bergen and Voss. 38
5.11 The posterior mean of the rutting from the common spatial field $\omega_{\mathrm{NS}}(s)$ for the spatial non-stationary model in drawn red, and from the common spatial field $\omega_{\mathrm{S}}(s)$ for the spatial stationary model in dashed blue. 39
5.12 The annual spatial deviation from the spatial field $\omega_{\mathrm{NS}}(s)$ for each of the years from 2017 to 2020 in drawn red, and from $\omega_{\mathrm{S}}(s)$ for each of the years from 2017 to 2020 in dashed blue. 40
5.13 The spatial range and marginal standard deviation for the spatial fields from the spatial non-stationary model as drawn lines, and from the spatial stationary model as dashed lines, as a function of the AADT. 41
5.14 The predicted rutting for year 2021 with a 95% credible interval, and on the map between Bergen and Voss. 42
5.15 The predicted standard deviation of the rutting for year 2021 for each road segment, and on the map between Bergen and Voss. . . 42
5.16 The predicted rut depth for year 2021 for each road segment, and on the map between Bergen and Voss. The road colored red on the right hand side is that which has an AADT of less than 5000, while the road colored black has an AADT of higher than 5000. A dotted red line is drawn at 25 millimeters of predicted rutting, while a dashed black line is drawn at 20 millimeters of predicted rutting. 43
5.17 The predicted rut depth with a 95% credible interval for the 200 first road segments from Bergen approaching Voss. 44

C.1 The rutting inferred from the common spatial field $\omega_{\mathrm{S}}(s)$ for the stationary model with a 95% credible interval and on the map between Bergen and Voss using sum-to-zero constraints. 52
C.2 The rutting inferred from the common spatial field $\omega_{\mathrm{NS}}(s)$ for the non-stationary model with a 95% credible interval and on the map between Bergen and Voss using sum-to-zero constraints. 53
C.3 The annual spatial deviation from the spatial field $\omega_{\mathrm{S}}(s)$ for each of the years from 2017 to 2020 using sum-to-zero constraints. . . . 54
C.4 The annual spatial deviation from the spatial field $\omega_{\mathrm{NS}}(s)$ for each of the years from 2017 to 2020 using sum-to-zero constraints. . . . 55

List of Tables

2.1 The summary statistic for the rutting in the years 2017 to 2020. . 7
2.2 The summary statistic for the rutting grouped by the AADT. . . . 12

5.1 The parameter estimates for the spatial non-stationary model for the rutting with a 95% credible interval. The median is reported for σ_γ and σ_ε, and the mean for the rest of the parameters. 31
5.2 The posterior parameter estimates for the non-spatial model for the rutting with a 95% credible interval. The median is reported for σ_γ and σ_ε, and the mean for the rest of the parameters. 34
5.3 The posterior parameter estimates for the spatial stationary model for the rutting with a 95% credible interval. The median is reported for σ_γ and σ_ε, and the mean for the rest of the parameters. 34
5.4 Model assessment criteria for the model with no spatial effects, the spatial stationary model, and the spatial non-stationary model. . . 41

B.1 The posterior parameter estimates for the spatial parameters for the spatial stationary model with a 95% credible interval. 50
B.2 The parameter estimates for the spatial parameters for the spatial non-stationary model with a 95% credible interval. 51

CHAPTER 1

Introduction

The project SMARTer maintenance (*SMARTere vedlikehold*) is a collaboration between the Norwegian Public Roads Administration (*Statens vegvesen*, NPRA), the Norwegian University of Science and Technology (NTNU), and NTNU Technology Transfer AS. This project aims to develop technology, methods and competence to improve and streamline maintenance of Norway's road network (Norwegian University of Science and Technology, 2022b). This Master's thesis considers the rutting, that is, the change in rut depth, along European route E16 between Bergen and Voss in the western most part of Norway. The aim is to locate effects responsible for increased rutting, and also to investigate whether spatial properties of the road impacts the rutting. In addition to spatial effects and yearly random effects, the traffic intensity, road cover type, and road width is used for inference and prediction of the rutting.

The road network in Norway had an estimated value of NOK 1600 billion in 2015 (Norwegian University of Science and Technology, 2022a), and the total cost to eliminate the maintenance backlog on the national and county road network lies between NOK 70 billion and NOK 115 billion (Sund, 2012; Sund, 2013). For the national road network, about 25 percent of this cost is related to pavements and draining, while the number is about 46 percent for the county road network. Over NOK 7 billion is spent annually for operation and maintenance of the national road network to ensure safety and accessibility (Norwegian Public Roads Administration, 2020). As the Norwegian road network falls under increasing strain from increased traffic intensity and challenging weather conditions, the roads lifetime could be reduced, and continuous maintenance is required.

Under ideal conditions, a solid pavement has an expected lifetime of between 20 and 30 years (Myre and Refsdal, 2005). Aurstad et al. (2016) finds that repavement occurs for Norwegian roads after around 15 years, which is between 5 and 15 years of pavement lost compared to ideal conditions. The rut depth (*spordybde*) is often used for measuring the condition of the surface of the pavement, and this is a measurement of the surface depression in the wheel path (Saba et al., 2006). These rut depths in the pavement may be caused by several factors, where we postulate that the traffic intensity, the road cover type, the road width, and spatial effects play a part. An increased rut depth prevents drainage, which causes hydroplaning and further deteriorates the road. We quantify the change in rut depth from the summer of one year to the summer of the next year, labeled as the rutting. The rutting for the year 2020 will then be defined as the change in rut depth between the summer of 2019 and the summer of 2020.

The study area is the European route E16 between Bergen and Voss, which constitutes about 80 kilometers of road. This road stretch is located in the western part of Norway, which is one of the places in Norway with the most annual precipitation. As increased water on the road decreases its lifetime (Aurstad et al., 2016), this stretch of road is suitable for the exploration of the rutting. The road stretch is divided into road segments of length 20 meters for which the rutting is calculated. The road measurements are measured by the NPRA, and Vedvik (2021) provided these for the years 2015 to 2020.

On the road in the study area, European route E16 between Bergen and Voss, there are three types of road cover, asphalt concrete (*asfaltbetong*, Ab), asphalt gravel concrete (*asfaltgrusbetong*, Agb), and stone mastic asphalt (*skjelettasfalt*, Ska). Usually asphalt concrete or stone mastic asphalt are used on roads with a high traffic intensity, while asphalt gravel concrete is used on roads with a low traffic intensity. There are several criteria for choosing the right road cover, including the traffic intensity, cost, access to materials, local conditions, and suitable properties such as noise, deformation and aging (Norwegian Public Roads Administration, 2022a). One would, according to spokespeople the NPRA, expect an increased rutting for the asphalt gravel concrete, compared to the two other road cover types.

The road width, which is the width of one lane of the road, also varies along the study area. With a low road width one would expect the vehicles driving on the road to lie in roughly the same position, giving more strain on this part of the road. With an increase in the road width the vehicles would be able to move more freely and use more of the width of the road. This would in turn result in the stress on the road being more distributed, and thus a lower rutting would be expected for a wider road.

Saba et al. (2006) showed that the observed average rutting increased with respect to an increasing traffic intensity. This is in accordance with Ebrahimi et al. (2019), which found that roads exposed to greater traffic volumes are more prone to shorter lifetimes. The traffic intensity is reported as the annual average daily traffic (AADT), which is defined as the average 24 hour traffic volume at a given location over a full 365 days per year (Molugaram and Rao, 2017). The AADT varies between the different road cover types and road widths, so looking at the interaction between the AADT and these other effects would be of interest.

According to guidelines, the maximum allowed rut depth is 25 millimeters for road stretches with an AADT of lower than 5000, while the maximum allowed rut depth is 20 millimeters for road stretches with an AADT of higher than 5000 before repaving (Norwegian Public Roads Administration, 2014). The rutting for 2021, for which there is no data available for us, will be predicted through the proposed model, and the results will be interpreted to determine whether repaving is necessary.

The use of studded tires on Alaskan roads was investigated by Lundy et al. (1992), and they found that the use of studded tires contribute greatly to the development of ruts in pavement. This, however, is difficult to quantify in this study, and is therefore not included. This also applies to the share of heavy traffic vehicles operating on the study area, where Sinkhonde and Ngoma (2020) found an increase in rutting with a higher share of heavy traffic vehicles. These two effects, among the other ones which are not explained, will then be explained through uncertainty in the model.

Svenson et al. (2016) considers roads in Sweden, using mixed proportional hazards models with random effects in addition to an intrinsic conditional autoregressive model to evaluate the spatial correlation between road segments. This resulted in the estimation that 17 percent of the unexplained variation in the lifetime between road segments was explained by the spatial correlation between the road segments. Another conclusion was that the spatial correlation between road segments existed up to 4 kilometers. Studies by Lea and Harvey (2015a) and Lea and Harvey (2015b) have also examined the spatial variability, which concluded with the correlation scale being less than approximately 50 meters.

The objective of this thesis is to develop a model for the rutting with uncertainty on Norwegian roads using available data from European route E16 between Bergen and Voss in the years 2015 to 2020. This may allow the NPRA to be able to identify areas for which the rutting is greater than expected, and also areas in need of repaving. Another objective is to investigate the spatial dependencies along the road, and whether this spatial dependence is stationary or non-stationary.

We propose three models for the rutting, where one is without spatial effects, and two includes spatial effects. The spatial effects are modeled as Gaussian random fields (GRFs), where we include one spatial field for each of the years 2017 to 2020 in the study period, and one time constant common spatial field. The framework introduced by Ingebrigtsen, Lindgren and Steinsland (2014) and Ingebrigtsen, Lindgren, Steinsland and Martino (2015) is used for including explanatory variables in the dependence structure of a GRF. We include the traffic intensity (AADT) to model the spatial non-stationarity.

For the non-spatial model, a Bayesian linear regression is preformed, while for the spatial models a Bayesian three-stage hierarchical model is used as latent Gaussian models (LGMs). A Gaussian random field (GRF) is included in the latent field in the LGM, making the model flexible. Through the stochastic partial differential equation (SPDE) approach to spatial modeling, the GRF is represented as a Gaussian Markov random field (GMRF) with Matérn covariance function (Lindgren, Rue and Lindström, 2011). This allows for the use of the integrated nested Laplace approximation (INLA), which is computationally superior to the more traditional Markov chain Monte Carlo (MCMC) methods (Rue, Martino and Chopin, 2009), implemented in the `R-INLA` package in `R`.

The rest of the text is organised as follows:

Chapter 2 consists of a description of the study area and an exploratory data analysis. The study area, the European route E16 between Bergen and Voss, is described including the road measurements, rutting, traffic intensity, road cover, and road width. An exploratory data analysis is then preformed where the variables are discussed in more detail, and spatial dependencies are discussed.

Chapter 3 introduces the mathematical background needed in the thesis. It introduces the concept of Bayesian statistics and latent Gaussian models (LGMs), before Gaussian random fields (GRFs) and Gaussian Markov random fields (GMRFs) are introduced. Laplace approximations, and a discussion around the integrated nested Laplace approximation (INLA) framework follows before the chapter concludes with the stochastic differential equation (SPDE) approach for spatial modeling, and an introduction of different model assessment criteria.

Chapter 4 describes the different statistical models for the rutting. A non-spatial model is first introduced, with a discussion of the choice of priors for the parameters. A model with fixed effects, random effects, and stationary GRFs is then introduced. The choice of priors for this model is then discussed. Then, a non-stationary model is introduced, where the non-stationarity is modeled as an effect of varying traffic intensity. The choice of priors for the non-stationary model is then discussed. Both spatial models are fitted as latent Gaussian models, where the stochastic partial differential equation method for spatial modeling ensures fast Bayesian inference using the integrated nested Laplace approximation framework. The chapter is concluded with a discussion of the inference and prediction of the models, and the software used, including a link to GitHub where relevant code and data can be found.

Chapter 5 shows the results of the models introduced in the previous chapter. The results of the rutting is presented for the fixed, random, and spatial effects, where parameter estimates are given with credible intervals. A comparison of the models are then given, looking at model selection criteria, the effect of adding spatial fields, and the effect of the non-stationarity. The chapter is concluded with a prediction of the rutting and rut depth of the European route E16 between Bergen and Voss for 2021 with uncertainty.

Chapter 6 gives a discussion, some concluding remarks, and some suggestions for further work.

Appendix A shows the methods for approximating the posterior marginals for the hyperparameters and the posterior marginals for the latent field for using the integrated nested Laplace approximation.

Appendix B lists the estimates of the parameters for the spatial effects for the stationary and non-stationary models. Credible intervals of the estimates are discussed, and also the reasonability of a non-stationary model compared to a stationary model.

Appendix C contains the results for the spatial effects of the spatial stationary and spatial non-stationary models when using a sum-to-zero constraint on the spatial effects. The reasonability of using this constraint is discussed, along with why we chose not to use it.

CHAPTER 2

Study Area, Data, and Exploratory Data Analysis

In this chapter, the study area and characteristics about the road measurements are presented. The rutting, traffic intensity, road cover type, and road width are discussed along the study area. The chapter concludes with an exploratory data analysis of the rutting with summary statistics, together with spatial variability, and the relation between the traffic intensity and road cover type.

2.1 European Route E16 Between Bergen and Voss

The study area is the European Route E16 between Bergen and Voss in the western part of Norway, in Vestland county, enclosed in the area shown in Figure 2.1. A map of the road is shown in Figure 2.7, and from this it is clear that the road lies in an area with a lot of fjords and mountains, an illustration of which is shown in Figure 2.2, where the road lies close to the fjord in mountainous terrain. The road in question is approximately 80 kilometers long, and lies mostly in rural areas with steep slopes. The road is divided into

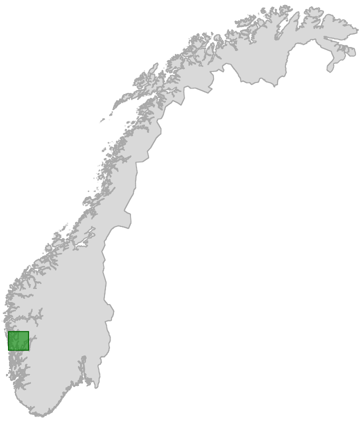

Figure 2.1: The study area, enclosed in the green box, is located in the western part of Norway, in Vestland county.

Figure 2.2: An illustration of the road on the European route E16 between Bergen and Voss. The road lies close to the fjord, and in mountainous terrain. (Photo: Øystein H. Brekke. Published: Wikimedia Commons.)

road segments of length 20 meters where the measurements are reported. This is the main road going east to west in Norway, and connecting Bergen to the capital Oslo.

2.2 Rutting

2.2.1 Data

The rut is a long track made by the repeated passage of the wheels of vehicles, and we consider the change in rut dept between each consecutive year as a metric for road deterioration. We quantify the change in rut depth from the summer of one year to the summer of the next year, labeled as the rutting. The rutting for the year 2020 will then be defined as the change in rut depth between the summer of 2019 and the summer of 2020. Letting d_{it} be the rut depth for road segment $i = 1, \ldots, n$ in year $t = 1, \ldots, T$, the rutting r_{it} is then defined as

$$r_{it} = d_{it} - d_{i,t-1},$$

for road segment $i = 1, \ldots, n$ in year $t = 1, \ldots, T$.

Data on the rutting for each segments and each year from 2015 to 2020 was provided courtesy of Vedvik (2021), however we use the rutting from year 2017 to 2020, which is obtained in the data cleaning described in Section 2.2.2. The density of the rutting for each of the years 2017 to 2020 is shown in Figure 2.3. From this the rutting for 2019 is larger than for the other years, and the variability also seams greatest for this year, while the rutting for 2020 has the lowest variability.

Performing a summary statistic on the rutting each year gives the results in Table 2.1. The mean of the rutting is largest in 2019, followed by 2017.

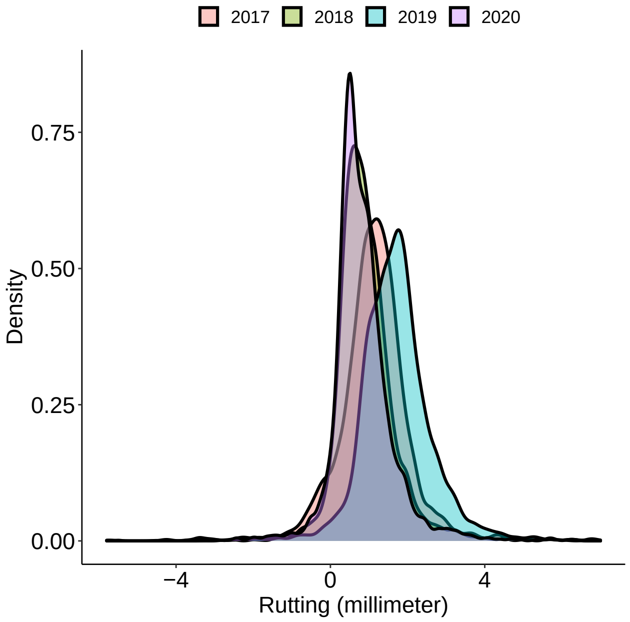

Figure 2.3: The density of the rutting for each of the years from 2017 to 2020.

Year	Mean	Standard deviation	Minimum	Maximum	Missing observations
2017	1.14	1.05	−5.7	12.4	1778
2018	0.96	0.92	−3.3	14.0	73
2019	1.77	1.20	−4.5	28.5	117
2020	0.84	0.89	−5.8	11.8	347

Table 2.1: The summary statistic for the rutting in the years 2017 to 2020.

The average annual rutting for each segment, and the corresponding density of this average rutting, over the years 2017 to 2020, is shown in Figure 2.4. The average annual rutting is mostly positive, and mostly lies below 2.5 millimeters. It is in general greater closer to Bergen with some spikes distributed along the road.

2.2.2 Cleaning of Data

Annual road condition measurements are made available for the years 2015 to 2020 along the European route E16 between Bergen and Voss courtesy of Vedvik (2021). These measurements measure the rut depth, and are made available each 20 meters.

The measurements does not start at the exact same location every year, and thus the measurements for the year 2020 is used as a basis for creating each of the road segments (Vedvik, 2021). For each of the years 2015 to 2019, the road segments corresponding to the road segment in 2020 is then found as the

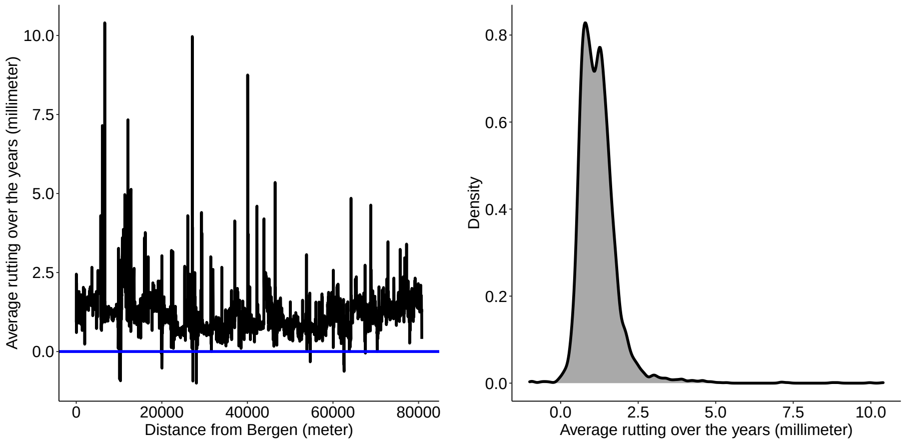

(a) The average annual rutting.

(b) The density.

Figure 2.4: The average annual rutting for each road segment, and the density of the average rutting, over the years 2017 to 2020.

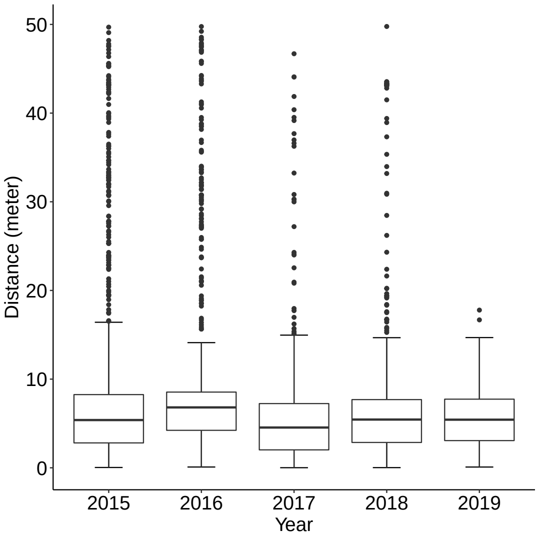

Figure 2.5: The Euclidean distance between the road segments in 2020 to those in 2015 to 2019.

one with the lowest Euclidean distance to the basis. If no errors are present this distance should not exceed 10 meters, but as Figure 2.5 shows, there are some larger distances, especially for the years 2015 to 2018. A visual inspection reveal that the reason for this may be that the road has been slightly altered during this period (Vedvik, 2021).

Summarizing the measurements, some are incomplete, namely those in 2015 and 2016. In the years from 2018 to 2020 there are 4032 road segments with valid measurements, while there is 4022 road segments with valid measurements in 2017. The European route E16 between Bergen and Voss consists of 4032 road segments in total, so for these years there is very little missing segments. For the years 2015 and 2016 however, there are 2600 and 2789 road segments with valid measurements, respectively. This corresponds to 35.4% and 30.8% missing segments. Thus, all the data presented in the following are based on the measurements from 2017 to 2020, and not including the years 2015 and 2016. This is the reason 2017 is the year with the most missing rutting observations in Table 2.1, because there are little data for the rut dept in 2016 to calculate the rutting in 2017.

The interest for road deterioration lies in positive values for the rutting, as negative values may occur from repaving or uncertainty in the measurements of the rut depth, coming from the position of the measurements or the measurements themselves. To separate out these values the filtering

$$r_{it} = \begin{cases} r_{it} & \text{if } r_{it} \geq -d_{it}/2, \\ \texttt{NaN} & \text{otherwise,} \end{cases}$$

is applied to the rutting. That is, if the rutting is at least half the rut depth the value is kept, otherwise the rutting for segment i in year t is set to a missing value. Performing this filtering on the data gives 2315 `NaN` values over all the years in the study period, constituting approximately 16.8% of the road segments.

The rut dept and the rutting for a subset of the study area[1] containing 250 road segments, constituting 5 kilometers, in proximity to Ytre Arna in Bergen municipality is shown in Figure 2.6. The rut dept increases for each year between 2017 and 2019, however, for large amounts of the road stretch, the rut dept decreases in 2020, indicating maintenance. Corresponding to these decreases in rut depth, the rutting is set to missing values, indicating that the filtering works as it should.

2.3 Traffic Intensity

The traffic intensity is measured in the annual average daily traffic (AADT), where different methods for calculating the AADT is discussed in Giæver and Johansen (2011). The AADT is extracted from Norwegian Public Roads Administration (2022b), and is reported as stretches of one kilometers of road with the same intensity, based on measuring points along the road. Figure 2.7 shows the AADT along the study area, and we observe a decrease in the AADT from west to east, with the lowest value of 4500 vehicles in the easternmost part close to Voss, and the highest value of 17200 vehicles close to Bergen in the west. The density of the different values of the AADT can be seen in Figure 2.8, and this shows that most of the road stretch has an AADT below 6000 vehicles.

The AADT is assumed to be equal for each of the years in the study period, and by manually checking the AADT at eleven measuring locations along the road, available for each of the years, the maximal difference in AADT is only between 5.9% and 13.4% (Norwegian Public Roads Administration, 2022b). This makes the assumption of equal traffic intensity for each of the years in the study period plausible.

---

[1] This subset has a high annual average daily traffic, ranging from 15000 to 17200 vehicles. Traffic intensity is discussed more in Section 2.3.

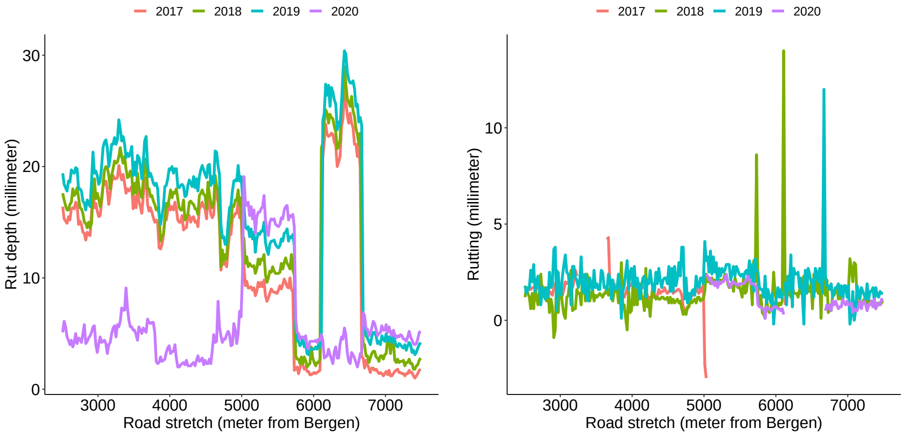

(a) The rut depth.

(b) The rutting.

Figure 2.6: The rut depth and rutting over the years 2017 to 2020 for a subset of the road containing 250 road segments in a high traffic intensity area in proximity to Ytre Arna in Bergen municipality.

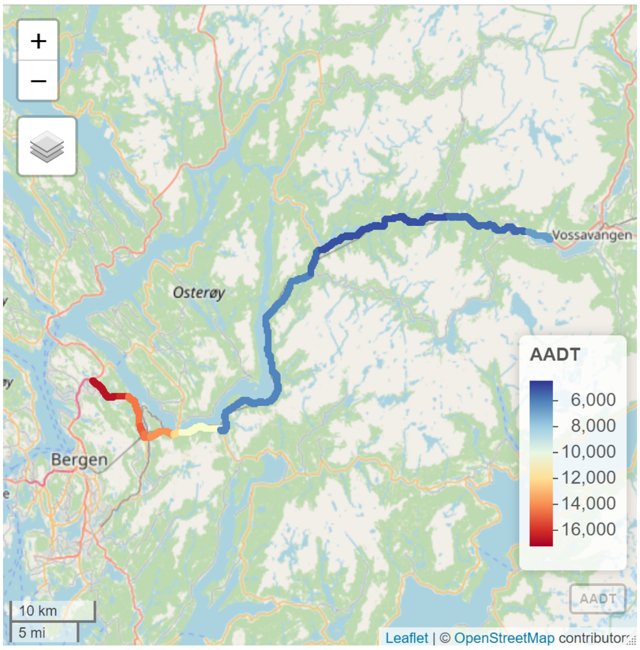

Figure 2.7: The AADT along the study area.

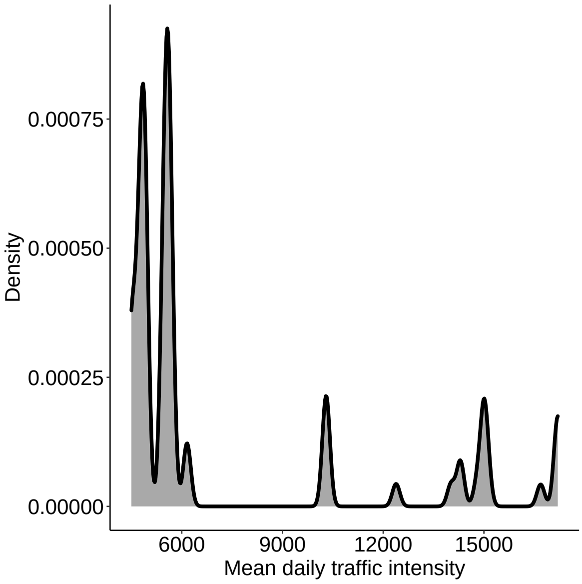

Figure 2.8: The mean daily traffic intensity.

2.4 Road Cover Type

The upper layer of the road surface is called the road cover, and for the European route E16 between Bergen and Voss there are three different road cover types (Norwegian Public Roads Administration, 2022b). These are shown in Figure 2.9, and are asphalt concrete (*asfaltbetong*, Ab), asphalt gravel concrete (*asfaltgrusbetong*, Agb), and stone mastic asphalt (*skjelettasfalt*, Ska). Most of the road is covered in asphalt concrete, while some smaller parts are covered in asphalt gravel concrete and stone mastic asphalt.

The road cover types are equal for the years in the study period, meaning that if maintenance occurred, the same road cover type was used for the same locations. According to the NPRA, the expectation is that there is more rutting for road cover type asphalt gravel concrete, than for the other two road cover types.

2.5 Road Width

The road width is the width of one lane, and for the study area it lies between 3.5 meters and 6.6 meters (Norwegian Public Roads Administration, 2022b). The road width is shown in Figure 2.10, where the road goes from Bergen to Voss on the first axis. From this we see that there are some parts of the road where there are missing data for the road width, that is about 10 kilometers from Bergen to about 20 kilometers from Bergen, and close to Voss. This missing data constitutes about 13.5% of the total amount of road segments. The expectation is that there is less rutting when the road is wide as the vehicles have more room to move sideways. This contrary to narrow roads where the

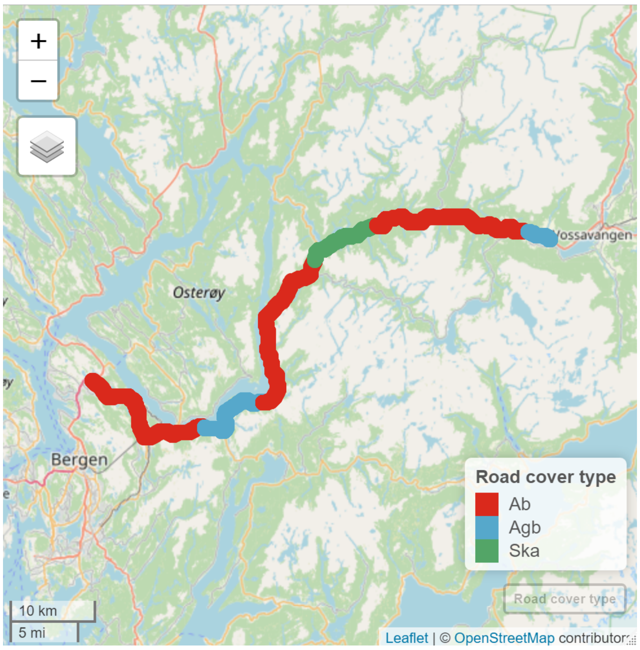

Figure 2.9: The three road covers in the study area, asphalt concrete (Ab), asphalt gravel concrete (Agb), and stone mastic asphalt (Ska).

AADT interval	Mean	Standard deviation	Number of segments
$[4500, 5000]$	0.90	1.06	3035
$[5000, 7040]$	0.82	1.14	3035
$(7040, 12100]$	1.37	1.15	247
$(12100, 14700]$	1.54	1.43	200
$(14700, 17200]$	1.21	1.19	548

Table 2.2: The summary statistic for the rutting grouped by the AADT.

vehicles have to lay in almost the same place, increasing the amount of stress on the pavement.

2.6 Exploratory Data Analysis

A summary statistic of the rutting using some intervals of the AADT as a grouping, is shown in Table 2.2. From this, there are most road segments having a low AADT, concurring with the observations in Section 2.3. The mean and standard deviation increases with the AADT, except for the decrease moving to the highest AADT interval. This is also shown in Figure 2.11, where the the rutting over all the years is shown using boxplots for the same intervals of the AADT.

Road cover type asphalt gravel concrete is typically used for road stretches with an AADT of less than 1500 vehicles, while for higher values of the AADT,

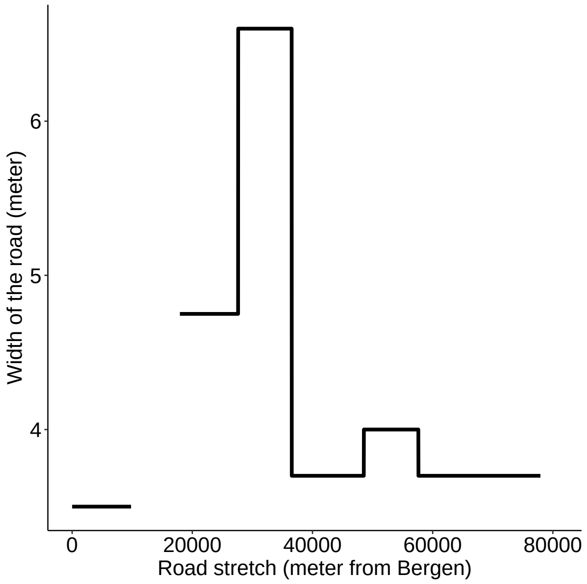

Figure 2.10: The road width along the road from Bergen to Voss.

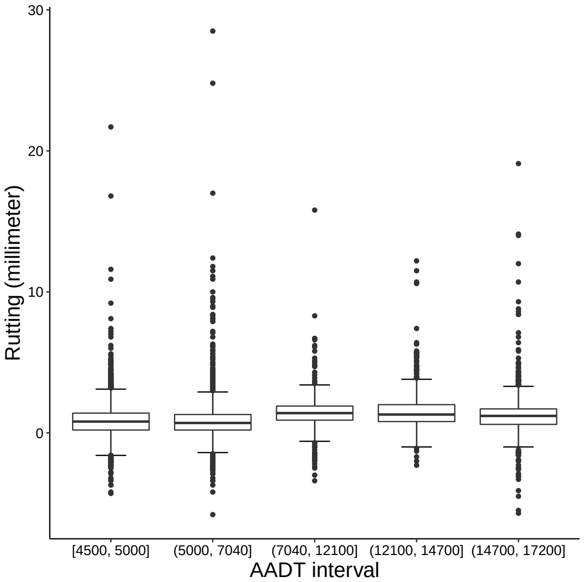

Figure 2.11: The rutting over all the years for some intervals of the AADT.

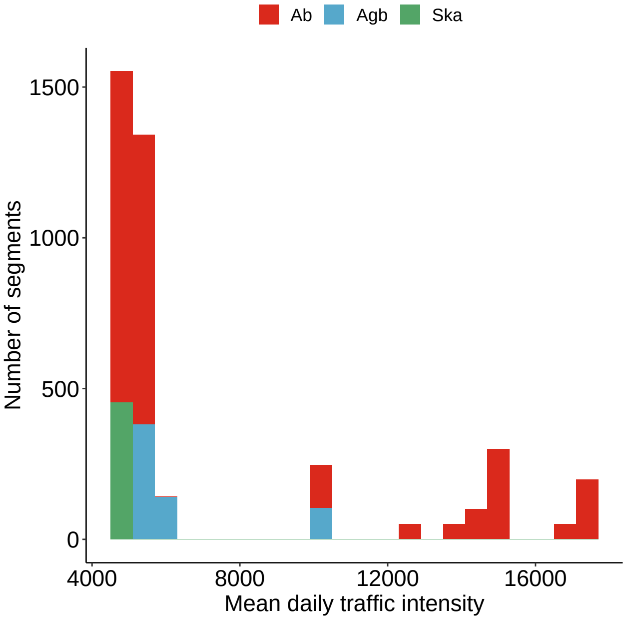

Figure 2.12: The number of road segments with different values of the AADT for each of the road cover types.

asphalt concrete and stone mastic asphalt is used (Norwegian Public Roads Administration, 2022a). Figure 2.12 shows how many segments there are that has a certain AADT for the different road cover types. This shows that the road cover type asphalt gravel concrete is used outside its regular usage here. For the road cover type stone mastic asphalt, the AADT is low, and it lies in the range 4500 to 4892. The other two road cover types are more spread out, and having a greater range of the AADT, this especially for road cover type asphalt concrete. Mainly for road cover type asphalt concrete and asphalt gravel concrete it would therefore be of interest to examine the interaction between the road cover type and the AADT.

A semivariogram, showing the spatial variability in the annual rutting, is shown in Figure 2.13 for the different years in the study period. From this, most of the variograms increase before level out at a short distance indicating spatial dependence, with the exception of the variogram for 2019 that has sudden spikes for the semivariance also for increasing distances. This is in agreement with Figure 2.3 and Table 2.1, where 2019 is shown to have a larger variance than the rest of the years.

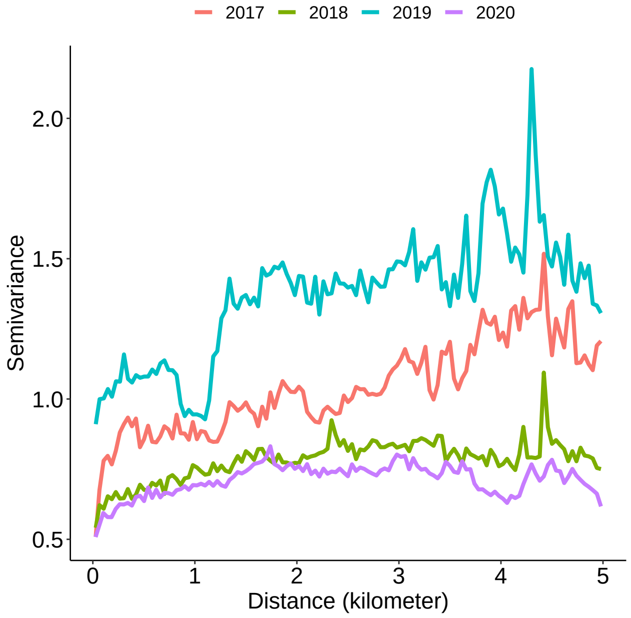

Figure 2.13: The variogram of the annual semivariance for rutting in the years 2017 to 2020.

CHAPTER 3

Background

In this chapter, the theoretical background needed to describe the statistical methods and models presented in Chapter 4 are introduced. The chapter starts with an introduction to Bayesian inference, and its application to latent Gaussian models (LGMs). Following this, Gaussian random fields (GRFs) are defined, and a brief explanation as to why Gaussian Markov random fields (GMRFs) are important is given. Laplace approximations, a central part of the integrated nested Laplace approximation (INLA) framework, is then described, before the INLA framework is covered. Theory around the stochastic partial differential equation (SPDE) approach to spatial models, is then presented, before some theory about different model assessment criteria is discussed.

3.1 Bayesian Inference

The Bayesian statistical domain treats the model parameters as unknown random variables, where in the frequentist framework these parameters are considered as fixed unknown values. Central in Bayesian inference is Bayes' theorem, where, following Givens and Hoeting (2012), the prior beliefs of the model parameter vector $\mathbf{x}$, given the vector of observed data $\mathbf{y}$, gives the posterior distribution of the model parameters as

$$p(\mathbf{x} \mid \mathbf{y}) = \frac{p(\mathbf{y} \mid \mathbf{x})p(\mathbf{x})}{p(\mathbf{y})},$$

where p described a probability mass function or a probability density function. The prior distribution is $p(\mathbf{x})$, which represents the prior belief, the likelihood function is $p(\mathbf{y} \mid \mathbf{x})$, and the marginal distribution of the data is $p(\mathbf{y})$. As the marginal distribution of the data is independent of $\mathbf{x}$, the factor $1/p(\mathbf{y})$ can be viewed as a normalizing constant. Thus, Bayes' theorem can be written in the form

$$p(\mathbf{x} \mid \mathbf{y}) \propto p(\mathbf{y} \mid \mathbf{x})p(\mathbf{x}), \tag{3.1}$$

Bayesian hierarchical models are often encountered in applications, and these are models where the parameters are defined on different stages. A three-stage hierarchical model consists of a likelihood function, a latent field[1], and priors for the hyperparameters (Blangiardo and Cameletti, 2015). This gives these

---

[1] In one dimension, a latent field is called a latent process.

models the form:

$$\begin{aligned}
\text{Likelihood:} \quad & \mathbf{y} \mid \mathbf{x}, \boldsymbol{\theta} \sim p(\mathbf{y} \mid \mathbf{x}, \boldsymbol{\theta}), \\
\text{Latent field:} \quad & \mathbf{x} \mid \boldsymbol{\theta} \sim p(\mathbf{x} \mid \boldsymbol{\theta}), \\
\text{Hyperparameters:} \quad & \boldsymbol{\theta} \sim p(\boldsymbol{\theta}).
\end{aligned}$$

In this case the vector of hyperparameters, $\boldsymbol{\theta}$, controls the priors of the model parameters, $p(\boldsymbol{\theta})$.

3.2 Latent Gaussian Models

It is for the class of latent Gaussian models (LGMs) that INLA is applicable, and we introduce this following Blangiardo and Cameletti (2015); Rue, Martino and Chopin (2009); Rue, Riebler et al. (2017). This introduction is also based on the preliminary work in Olsen (2021). The LGMs is a class of Bayesian three-stage hierarchical models consisting of a likelihood model, a latent Gaussian field, and a vector of hyperparameters. The data $\mathbf{y}$ is also assumed to be conditionally independent given the latent Gaussian field $\mathbf{x}$. The mean $\mu_i = \mathrm{E}(y_i)$ is connected to a Gaussian linear predictor η_i through a link function g, such that $g(\mu_i) = \eta_i$. Given that μ is the overall intercept, $\mathbf{x}$ are fixed covariates with linear effects $\{\beta_j\}$, and the ε_i's are unstructured terms, this linear predictor is additive having the form

$$\eta_i = \mu + \sum_{j=1}^{n_\beta} \beta_j x_{ij} + \sum_{k=1}^{n_f} f^{(k)}(u_{ik}) + \varepsilon_i.$$

The terms $\{f^{(k)}\}$ model specific random effects of the covariate $\mathbf{u}$, and thus takes many different forms, for example as a spatial random effect using the SPDE method, as described in Section 3.6.

For LGMs we assume that the latent field has a Gaussian prior with mean $\mathbf{0}$ and precision matrix[2] $Q(\boldsymbol{\theta})$. This, in addition to the conditional independence of the data, gives the three-stage hierarchical model

$$\begin{aligned}
\text{Likelihood:} \quad & \mathbf{y} \mid \boldsymbol{\eta}, \boldsymbol{\theta} \sim \prod_{i=1}^{n} p(y_i \mid \eta_i, \boldsymbol{\theta}), \\
\text{Latent field:} \quad & \boldsymbol{\eta} \mid \boldsymbol{\theta} \sim \mathrm{Normal}(\mathbf{0}, Q(\boldsymbol{\theta})^{-1}), \\
\text{Hyperparameters:} \quad & \boldsymbol{\theta} \sim p(\boldsymbol{\theta}).
\end{aligned} \tag{3.2}$$

This Gaussian assumption of the latent field only applies there, and not to the hyperparameters, meaning that $p(\boldsymbol{\theta})$ may be any suitable prior distribution. Using Bayes' theorem in Equation (3.1) and all the stages in the Bayesian three-stage hierarchical model in Equation (3.2) gives the joint distribution of the latent field and the hyperparameters, having the form

$$\begin{aligned}
p(\boldsymbol{\eta}, \boldsymbol{\theta} \mid \mathbf{y}) &\propto p(\boldsymbol{\theta}) p(\boldsymbol{\eta} \mid \boldsymbol{\theta}) p(\mathbf{y} \mid \boldsymbol{\eta}, \boldsymbol{\theta}) \\
&\propto p(\boldsymbol{\theta}) |\det(Q(\boldsymbol{\theta}))|^{1/2} \exp\left(-\frac{1}{2} \boldsymbol{\eta}^\top Q(\boldsymbol{\theta}) \boldsymbol{\eta} + \sum_{i=1}^{n} \ln(p(y_i \mid \eta_i, \boldsymbol{\theta})) \right).
\end{aligned}$$

This form follows from the known density of the $\mathrm{Normal}(\mathbf{0}, Q(\boldsymbol{\theta})^{-1})$ distribution.

---

[2] The precision matrix of a random variable is the inverse of the covariance matrix.

3.3 Gaussian Random Fields

Gaussian random fields (GRFs) is the most important class of random fields, and our coverage is based on Blangiardo and Cameletti (2015). A GRF is a spatial process $\{\xi(\mathbf{s}) : \mathbf{s} \in \mathcal{D} \subseteq \mathbb{R}^d\}$ that for any $n \geq 1$ and for each set of spacial locations $(\mathbf{s}_1, \ldots, \mathbf{s}_n)$ satisfies

$$\boldsymbol{\xi} = (\xi(\mathbf{s}_1), \ldots, \xi(\mathbf{s}_n)) = (\xi_1, \ldots, \xi_n) \sim \text{Normal}(\boldsymbol{\mu}, \Sigma).$$

Here $\boldsymbol{\mu} = (\mu(\mathbf{s}_1), \ldots, \mu(\mathbf{s}_n))$ is the mean vector, while $\Sigma_{ij} = \text{Cov}(\xi(\mathbf{s}_i), \xi(\mathbf{s}_j)) = C(\xi(\mathbf{s}_i), \xi(\mathbf{s}_j))$ are the elements of the covariance matrix defined by some[3] covarance function C. It is the covariance function that defines the structure of the GRF.

The spatial process is said to be second-order stationary if for all i, the mean is constant, $\mu(\mathbf{s}_i) = \mu$, and $\text{Cov}(\xi(\mathbf{s}_i), \xi(\mathbf{s}_j)) = \mathcal{C}(\mathbf{s}_i - \mathbf{s}_j)$. If, instead, $\text{Cov}(\xi(\mathbf{s}_i), \xi(\mathbf{s}_j)) = \mathcal{C}(\|\mathbf{s}_i - \mathbf{s}_j\|_2)$, then the spatial process is isotropic, and we will see that the Matérn covariance function defined in Equation (3.7) is stationary and isotropic.

3.3.1 Gaussian Markov Random Fields

Replacing the GRF with a Gaussian Markov random field (GMRF) helps with computational efficiency, and has a wide area of applications, including for the SPDE approach for GRFs in Section 3.6. For an in depth introduction to GMRFs the reader is referred to Gelfand et al. (2010); Rue and Held (2005).

The introduction of GMRFs gives great advantages in computational time. If one were to preform the Cholesky factorization $Q = LL^\top$ of a precision matrix $Q \in \mathbb{R}^{n \times n}$ it would normally take $\mathcal{O}(n^3)$ flops[4], while for spatial GMRFs a sparse[5] Q will reduce this to $\mathcal{O}(n^{3/2})$ in two dimensions, and only $\mathcal{O}(n)$ in one dimension, as is the case in this thesis (Rue, Martino and Chopin, 2009). So the computational efficiency of GMRFs are obtained when the precision matrix is sufficiently sparse.

3.4 The Laplace Approximation

The use of nested Laplace approximations are central in the INLA framework, and it is here introduced following Blangiardo and Cameletti (2015). Here, we are interested in computing an integral of the form

$$\int f(x)\,\mathrm{d}x = \int \exp(\ln(f(x)))\,\mathrm{d}x, \tag{3.3}$$

where $f(x)$ is the probability density function of a random variable. Taylor expanding around $x = x_0$, and approximating to the second order, gives

$$\ln(f(x)) \approx \ln(f(x_0)) + (x - x_0)\frac{\partial \ln(f(x))}{\partial x}\bigg|_{x=x_0} + \frac{1}{2}(x - x_0)^2 \frac{\partial^2 \ln(f(x))}{\partial x^2}\bigg|_{x=x_0}.$$

---

[3] For example, the Matérn covariance function defined in Equation (3.7).

[4] Floating point operations per second (flops) is a much used measure for computer performance.

[5] A criterion that can be used for a matrix in $\mathbb{R}^{n \times n}$ to be sparse, is that only $\mathcal{O}(n)$ of the n^2 entries are non-zero (Rue, Martino and Chopin, 2009).

The mode $x^* = \arg\max_x\{\ln(f(x))\}$ can be computed iteratively by the scoring algorithm (Rue, Martino and Chopin, 2009), and setting x_0 equal to the mode ensures that the first derivative is zero. The integral of interest can thus be approximated as

$$\int f(x)\,\mathrm{d}x \approx f(x^*) \int \exp\left(\frac{1}{2}(x-x^*)^2 \frac{\partial^2 \ln(f(x))}{\partial x^2}\bigg|_{x=x^*}\right) \mathrm{d}x.$$

The integrand here can then be associated with the density of a normal distribution, and letting

$$(\sigma^2)^* := -\left(\frac{\partial^2 \ln(f(x))}{\partial x^2}\bigg|_{x=x^*}\right)^{-1},$$

we can write

$$\int f(x)\,\mathrm{d}x \approx f(x^*) \int \exp\left(\frac{(x-x^*)^2}{2(\sigma^2)^*}\right) \mathrm{d}x.$$

Thus, the integrand is the kernel of a normal distribution with mean being the mode x^* and variance $(\sigma^2)^*$. It then follows that the integral in Equation (3.3) evaluated in the interval $[a,b]$ can be approximated as

$$\int_a^b f(x)\,\mathrm{d}x \approx f(x^*)\sqrt{2\pi(\sigma^2)^*}(\Phi(b)-\Phi(a)),$$

where Φ is the cumulative density function of the Normal$(x^*, (\sigma^2)^*)$ distribution.

3.5 Integrated Nested Laplace Approximations

We introduce the framework of the deterministic integrated nested Laplace approximation (INLA) approach for doing approximate Bayesian inference for latent Gaussian models. INLA is fast for large and complex models, and does not suffer from slow convergence or poor mixing. It then proves better than Markov chain Monte Carlo (MCMC) methods computationally. INLA is implemented in the `R` package `R-INLA` returning posterior marginals for all the model parameters with summary information. This introduction to INLA is based on Blangiardo and Cameletti (2015); Martino and Riebler (2019); Moraga (2019); Rue, Martino and Chopin (2009); Rue, Riebler et al. (2017).

In the INLA framework, the variables μ, $\boldsymbol{\beta}$ and $f^{(k)}$ for $k = 1,\dots,n_f$, introduced in Section 3.2, are assigned Gaussian priors. Then

$$\mathbf{x} = \{\boldsymbol{\eta}, \mu, \boldsymbol{\beta}, f^{(1)}, f^{(2)}, \dots, f^{(n_f)}\},$$

is a latent Gaussian field. When performing Bayesian inference with INLA on LGMs, the interest lies in computing the posterior marginals for the hyperparameters

$$p(\theta_j \mid \mathbf{y}) = \iint p(\mathbf{x}, \boldsymbol{\theta} \mid \mathbf{y})\,\mathrm{d}\mathbf{x}\,\mathrm{d}\boldsymbol{\theta}_{-j} = \int p(\boldsymbol{\theta} \mid \mathbf{y})\,\mathrm{d}\boldsymbol{\theta}_{-j},$$

for $j = 1,\dots,\dim(\boldsymbol{\theta})$, in addition to the posterior marginals of the latent field

$$p(x_i \mid \mathbf{y}) = \iint p(\mathbf{x}, \boldsymbol{\theta} \mid \mathbf{y})\,\mathrm{d}\mathbf{x}_{-i}\,\mathrm{d}\boldsymbol{\theta} = \int p(x_i, \boldsymbol{\theta} \mid \mathbf{y}) p(\boldsymbol{\theta} \mid \mathbf{y})\,\mathrm{d}\boldsymbol{\theta},$$

for $i = 1, \dots, n$. This approach is only applicable for LGMs where $\dim(\boldsymbol{\theta})$ is small, or else the computational time gets to big. Also $\mathbf{x} \mid \boldsymbol{\theta}$ must be a GMRF, and the likelihood must be conditionally independent in the sense that y_i only depends on $\boldsymbol{\theta}$ and one x_i. The goal is then to build the nested approximations

$$\tilde{p}(\theta_j \mid \mathbf{y}) = \int \tilde{p}(\boldsymbol{\theta} \mid \mathbf{y}) \, \mathrm{d}\boldsymbol{\theta}_{-j}, \tag{3.4}$$

and

$$\tilde{p}(x_i \mid \mathbf{y}) = \int \tilde{p}(x_i, \boldsymbol{\theta} \mid \mathbf{y}) \tilde{p}(\boldsymbol{\theta} \mid \mathbf{y}) \, \mathrm{d}\boldsymbol{\theta}, \tag{3.5}$$

with $\tilde{p}$ being the approximate densities. The approach is to first construct an approximation of the posterior marginals for the hyperparameters, and then an approximation of the posterior marginals for the latent field. These approximations are shown in Appendix A.

3.6 The Stochastic Partial Differential Equation Approach to Spatial Modeling

The stochastic partial differential equation (SPDE) approach to spatial modeling was introduced by Lindgren, Rue and Lindström (2011) and it is used to represent a GRF as a GMRF. The main advantage with this approach is that the properties of the GRF is characterised by an SPDE and not a covariance function. Thus the SPDE can be modified to obtain GRFs with other dependence structures. Here we introduce this concept for both stationary and non-stationary SPDEs. In addition to the original paper we also use Blangiardo and Cameletti (2015); Ingebrigtsen, Lindgren and Steinsland (2014); Ingebrigtsen, Lindgren, Steinsland and Martino (2015); Krainski et al. (2019) to describe both the stationary and non-stationary case of the SPDE approach.

3.6.1 Stationarity

The linear fractional stationary stochastic partial differential equation has the form

$$(\kappa^2 - \Delta)^{\alpha/2}(\tau \xi(\mathbf{s})) = \mathcal{W}(\mathbf{s}), \tag{3.6}$$

where $\mathbf{s} \in \mathcal{D} \subseteq \mathbb{R}^d$, Δ is the Laplacian, α controls the smoothness, κ is the scale parameter, τ controls the variance, and $\mathcal{W}(\mathbf{s})$ is a Gaussian spatial white noise process. The solution to this SPDE is the stationary GRF $\xi(\mathbf{s})$ having the Matérn stationary isotropic covariance function

$$C(\xi(\mathbf{s}_i), \xi(\mathbf{s}_j)) = \frac{\sigma^2}{2^{\nu-1}\Gamma(\nu)} (\kappa \|\mathbf{s}_i - \mathbf{s}_j\|_2)^\nu K_\nu(\kappa \|\mathbf{s}_i - \mathbf{s}_j\|_2), \tag{3.7}$$

for $\mathbf{s}_i, \mathbf{s}_j \in \mathcal{D}$, where $\| \cdot \|_2$ denotes the Euclidean distance. Here σ^2 is the marginal variance, $\kappa > 0$ is a scaling parameter, and K_ν is the modified Bessel function of the second kind and order $\nu > 0$.

Following Lindgren, Rue and Lindström (2011) the link between the parameters in the SPDE in Equation (3.6) and the parameters in the Matérn covariance function in Equation (3.7) is

$$\nu = \alpha - \frac{d}{2} \quad \text{and} \quad \sigma^2 = \frac{\Gamma(\nu)}{(4\pi)^{d/2}\Gamma(\alpha)\kappa^{2\nu}\tau^2}.$$

However, instead of using the scaling parameter κ, it is common to use the spatial range parameter ρ, defined empirically as $\rho = 2\sqrt{2\nu}/\kappa$. This range corresponds to the distance where the spatial correlation is close to 0.13 for $\nu > 1/2$. We consider the case where $d = 1$, and $\alpha = 2$ is the default value in `R-INLA`, such that $\nu = 3/2$ and

$$\rho = \frac{2\sqrt{3}}{\kappa} \quad \text{and} \quad \sigma^2 = \frac{1}{4\kappa^3\tau^2}. \tag{3.8}$$

These are the values for d and α we consider in this thesis, and will be used from this point.

To set priors the penalised complexity (PC) prior framework in Simpson et al. (2017), giving informative priors, is used. This framework is extended in Fuglstad et al. (2017) to set joint priors for the spatial range ρ and the marginal standard deviation σ of GRFs with Matérn covariance functions.

Using the finite element method[6] on a triangulation of the domain $\mathcal{D}$ yields the approximation

$$\xi(\mathbf{s}) = \sum_{i=1}^{V} w_i \varphi_i(\mathbf{s}), \tag{3.9}$$

where V is the total number of vertices of the triangulation, $\{\varphi_i(\mathbf{s})\}$ is the set of basis functions, and $\{w_i\}$ are zero-mean Gaussian distributed weights. Lindgren, Rue and Lindström (2011) made the choice that the weights determine the values of the field at the vertices. That is, we let φ_i be piece-wise linear in each triangle, letting it be 1 at vertex i, and 0 at all other vertices.

Define the diagonal matrix R and the sparse matrix S with elements

$$R_{ii} = \int \varphi_i(\mathbf{s})\,\mathrm{d}\mathbf{s} \quad \text{and} \quad S_{ij} = \int \nabla\varphi_i(\mathbf{s})\nabla\varphi_j(\mathbf{s})\,\mathrm{d}\mathbf{s},$$

for $i, j = 1, \ldots, V$. Using Neumann boundary conditions leads to

$$Q_{\mathrm{S}} = \tau^2(\kappa^4 R + 2\kappa^2 S + SR^{-1}S), \tag{3.10}$$

being the precision matrix for the weights $\mathbf{w} = (w_1, \ldots, w_V)$. Then the finite dimensional solution to the SPDE in Equation (3.6) also has precision matrix Q_{S}, and because of the sparsity of this we obtain a GMRF model.

3.6.2 Non-Stationarity

When modeling different natural phenomena, the stationary assumption may not be suitable, as it may be inappropriate to assume for example the spatial correlation to be constant. The following discussion of non-stationarity is based on Ingebrigtsen, Lindgren and Steinsland (2014); Ingebrigtsen, Lindgren, Steinsland and Martino (2015). Letting κ and τ in the SPDE in Equation (3.6) vary based on the spatial location $\mathbf{s}$ gives the non-stationary SPDE

$$(\kappa(\mathbf{s})^2 - \Delta)^{\alpha/2}(\tau(\mathbf{s})\xi(\mathbf{s})) = \mathcal{W}(\mathbf{s}), \tag{3.11}$$

where the variables has the same meaning as in Equation (3.6), just that κ and τ are dependent on $\mathbf{s}$. This makes the solutions $\xi(\mathbf{s})$ non-stationary GRFs because

---

[6] An introduction to the finite element method can be found in Brenner and Scott (2008).

the correlation range and variance will vary with location. The parameters $\kappa(\mathbf{s})$ and $\tau(\mathbf{s})$ can be defined log-linearly as

$$\ln(\kappa(\mathbf{s})) = \theta_1^{(\kappa)} + \sum_{i=2}^{N} \theta_i^{(\kappa)} b_i^{(\kappa)}(\mathbf{s}) \quad \text{and} \quad \ln(\tau(\mathbf{s})) = \theta_1^{(\tau)} + \sum_{i=2}^{N} \theta_i^{(\tau)} b_i^{(\tau)}(\mathbf{s}),$$

where the $\{\theta_i^{(\cdot)}\}$ are weight parameters for which priors are specified and $\{b_i^{(\cdot)}(\mathbf{s})\}$ are basis functions defined on $\mathcal{D}$.

The precision matrix in Equation (3.10) is in the non-stationary case modified to

$$Q_{\text{NS}} = T(K^2RK^2 + K^2S + SK^2 + SR^{-1}S)T, \tag{3.12}$$

where T and K are diagonal matrices with elements $T_{ii} = \tau(\mathbf{s}_i)$ and $K_{ii} = \kappa(\mathbf{s}_i)$, for $i = 1, \dots, V$. It will thus still be sparse, and the finite dimensional solution to the SPDE in Equation (3.11) has precision matrix Q_{NS}, and we obtain a GMRF model.

In the non-stationary case, Equation (3.8) is no longer valid. However, the link between the SPDE and the Matérn parameters can be approximated as

$$\rho(\mathbf{s}) \approx \frac{2\sqrt{3}}{\kappa(\mathbf{s})} \quad \text{and} \quad \sigma(\mathbf{s})^2 \approx \frac{1}{4\kappa(\mathbf{s})^3\tau(\mathbf{s})^2}, \tag{3.13}$$

for slowly varying $\kappa(\mathbf{s})$ and $\tau(\mathbf{s})$ (Ingebrigtsen, Lindgren and Steinsland, 2014).

3.7 Model Assessment

Comparing different models to each other requires different model selection criteria, and we introduce three of these. They are the deviance information criteria, the Watanabe-Akaike information criterion, and lastly the marginal log-likelihood.

The deviance information criterion (DIC) was proposed by Spiegelhalter et al. (2002), and is a hierarchical modeling generalization of the Akaike information criterion (Akaike, 1974). In Bayesian statistics, DIC is widely used to perform model selection, and the value is determined both by the model fit and the model complexity. For a model with likelihood $p(\mathbf{y} \mid \boldsymbol{\eta}, \boldsymbol{\theta})$, the deviance is defined as

$$D(\boldsymbol{\eta}, \boldsymbol{\theta}) = -\ln(p(\mathbf{y} \mid \boldsymbol{\eta}, \boldsymbol{\theta})).$$

The posterior expectation of the deviance is $\bar{D} = \mathrm{E}_{\boldsymbol{\eta},\boldsymbol{\theta}|\mathbf{y}}(D(\boldsymbol{\eta}, \boldsymbol{\theta}))$, and using this, the model complexity is measured as

$$p_{\text{DIC}} = \bar{D} - D(\mathrm{E}_{\boldsymbol{\eta},\boldsymbol{\theta}|\mathbf{y}}(\boldsymbol{\eta}, \boldsymbol{\theta})).$$

From this the deviance information criterion is defined as

$$\text{DIC} = p_{\text{DIC}} + \bar{D},$$

and models with smaller DIC should be preferred over models with larger DIC.

The Watanabe-Akaike information criterion[7] (WAIC) is the generalized version of the Akaike information criterion (AIC) (Watanabe, 2010). This is a

---

[7] The Watanabe-Akaike information criterion is also often known as the widely applicable information criterion.

more fully Bayesian approach to estimating the expectation of the posterior log-likelihood, and then penalising for overfitting by adding a term for the effective number of parameters. Following Yong (2018), we define the log point-wise predictive density as

$$\mathrm{LPPD} = \sum_{i=1}^{n} \ln \left(\int p(y_i \mid \boldsymbol{\theta}) p(\boldsymbol{\theta}) \, \mathrm{d}\boldsymbol{\theta} \right),$$

where $p(\boldsymbol{\theta})$ is the whole posterior density. The penalty term modeling the models complexity can be expressed as

$$p_{\mathrm{WAIC}} = \sum_{i=1}^{n} \mathrm{Var}(\ln(p(y_i \mid \boldsymbol{\theta}))),$$

with the variance being the posterior variance. The WAIC is then defined as

$$\mathrm{WAIC} = 2p_{\mathrm{WAIC}} - 2\mathrm{LPPD}.$$

Models with a smaller WAIC should be preferred to models with a larger WAIC. For an in-depth discussion of DIC and WAIC the reader is referred to Gelman, Hwang and Vehtari (2014).

INLA computes an approximation to the marginal likelihood by marginalizing

$$\tilde{p}(\mathbf{y}) = \int \left. \frac{p(\mathbf{y}, \mathbf{x}, \boldsymbol{\theta})}{\tilde{p}(\mathbf{x} \mid \mathbf{y}, \boldsymbol{\theta})} \right|_{\mathbf{x}=\mathbf{x}^*(\boldsymbol{\theta})} \mathrm{d}\boldsymbol{\theta},$$

using the approximation in Equation (3.5). Hubin and Storvik (2016) showed that INLA gives reliable approximations, also compared to other approaches of approximation. The marginal log-likelihood is then found by $\ln(\tilde{p}(\mathbf{y}))$, and we prefer models with larger marginal log-likelihood values to those with smaller values.

CHAPTER 4

Statistical Models and Methods for Rutting

In this chapter we propose models for the rutting consisting of fixed effects and random effects along the road. One model without spatial effects, and two different spatial models are introduced, having either stationary or non-stationary spatial fields. These models are fitted in a Bayesian framework using INLA, where the likelihood family is assumed a zero-mean Gaussian. This is done to find the different effects of the covariates on the expected rutting, and also to check for spatial effects. The chapter starts with a presentation of the statistical models, and how priors for these models are chosen. Some discussion of the triangulation used for the SPDE approach is also given. The chapter is concluded with a brief description of the software used for the inference and prediction.

4.1 The Latent Gaussian Models for Rutting

We denote by $\mathcal{R} \subset \mathbb{R}$ the spatial domain of the road, in which we assume the road to be one dimensional. Thus, $s \in \mathcal{R}$ denotes a location along the road of interest. In year t, the linear predictor $\eta_t(s_i)$ includes both the fixed effects and the random effects for segment s_i, and the spatial process $\{\eta_t(s) : s \in \mathcal{R}\}$ describes the rutting along the road. The rutting r_{it} for segment $i = 1, \ldots, n$ and year $t = 1, \ldots, T$ is then given by the relation

$$r_{it} = \eta_t(s_i) + \varepsilon_{it},$$

where the residuals are assumed $\varepsilon_{it} \overset{\text{i.i.d.}}{\sim} \text{Normal}(0, \tau_\varepsilon^{-1})$, where $\tau_\varepsilon = \sigma_\varepsilon^{-2}$ is the precision parameter. The road segments i, for which the rutting is calculated are, as discussed in Section 2.1, discretized to 20 meters of road. For simplicity's sake, each of these road segments are treated as points, and not lines, where s_i denotes the midpoint of road segment i.

It is within the linear predictor $\eta_t(s)$ where the models differ, and all fixed effects and random effects are included here. The spatial effects are the elements of the linear predictor which is described by a Gaussian random field, which can be stationary or non-stationary. In the next sections, we describe a model without spatial effects, a model with stationary spatial effects, and a model with non-stationary spatial effects.

4.2 The Model Without Spatial Effects

The model without spatial effects has the linear predictor

$$\eta_t(s) = \beta_{\text{Ab}} x_{\text{Ab}} + \beta_{\text{Agb}} x_{\text{Agb}} + \beta_{\text{Ska}} x_{\text{Ska}} + \beta_{\text{w}} x_{\text{w}} + \gamma_t,$$

where the covariates $x_{\cdot} = x_{\cdot}(s)$, but the dependence on the location s is suppressed to increase readability. The covariate x_{Ab} is the value of the AADT if the road cover is asphalt concrete, and zero otherwise. Similarly for x_{Agb} and x_{Ska}, with the respective road cover types asphalt gravel concrete and stone mastic asphalt. We include this as a covariate as there is reason to believe that different road cover types gives different properties to the road. This could then lead to different amounts of rutting for different road cover types. The covariate x_{w} is the width of the road interacting with the AADT, and is a continuous covariate. As discussed earlier it is reasonable to think that the road width affects the rutting. This is because if the road is narrower the vehicles have less possibility to move within its lane, and the wheels would be more concentrated at the same location in the lane, leading to more stress on the pavement here. We assume the random yearly effects are distributed as $\boldsymbol{\gamma} = (\gamma_1, \ldots, \gamma_T) \sim \text{Normal}(\mathbf{0}_T, \tau_\gamma^{-1} I_T)$, where $I_T \in \mathbb{R}^{T \times T}$ is the identity matrix, and $\mathbf{0}_T \in \mathbb{R}^T$ is the zero-vector. The hyperparameter is assigned the prior $\tau_\gamma \sim \text{Gamma}(0, 5 \cdot 10^{-5})$, and is assigned as such as we have no prior knowledge about this parameter. The plot of the annual empirical rutting in Figure 2.3 shows a difference in the rutting for each year, justifying this as an effect. The yearly effect is included as a random effect because this allows for easier prediction.

The fixed effects are assigned vague Gaussian priors, where $\boldsymbol{\beta} = (\beta_{\text{Ab}}, \beta_{\text{Agb}}, \beta_{\text{Ska}}, \beta_{\text{w}}) \overset{\text{i.i.d.}}{\sim} \text{Normal}(0, 1000)$. The hyperparameter for the residuals is assigned the prior $\tau_\varepsilon \sim \text{Gamma}(0, 5 \cdot 10^{-5})$, where, as for the prior for the hyperparameter for the random yearly effect, this prior is is assigned as such because we have no prior knowledge about this parameter.

4.3 Spatial Stationary Model for Rutting

For the spatial stationary model the linear predictor takes the form

$$\eta_{t,\text{S}}(s) = \beta_{\text{Ab}} x_{\text{Ab}} + \beta_{\text{Agb}} x_{\text{Agb}} + \beta_{\text{Ska}} x_{\text{Ska}} + \beta_{\text{w}} x_{\text{w}} + \gamma_t + \omega_{\text{S}}(s) + \xi_{t,\text{S}}(s),$$

where the subscript S symbolises the stationarity of the linear predictor and the GRFs. The fixed effects has the same interpretation as for the model with no spatial effects. The spatial field $\omega_{\text{S}}(s)$ is a common field constant in time, while $\xi_{t,\text{S}}(s)$ for $t = 1, \ldots, T$ is an annually varying spatial field which may be effected by for example weather conditions. Thus, $\xi_{t,\text{S}}(s)$ describes the annual spatial deviation from the spatial field $\omega_{\text{S}}(s)$ in accordance with Ingebrigtsen, Lindgren, Steinsland and Martino (2015). The reason for including spatial fields follows from the semivariogram in Figure 2.13, which indicates spatial effects. It is also expected that different parts of the road experiences different amounts of rutting based on possible spatial patterns in weather or heavy traffic.

The spatial dependencies $\omega_{\text{S}}(s)$ and $\xi_{t,\text{S}}(s)$ for $t = 1, \ldots, T$ are modeled as GRFs with Matérn covariance functions, and thus the SPDE approach from

Section 3.6 can be applied. This requires a triangulation of the domain $\mathcal{R}$, where the basis functions of the GRF is defined. As the spatial domain is one-dimensional, the triangulation has a vertex every 20^{th} meter. This means that each triangle covers one road segment, and due to $\mathcal{R}$ being one-dimensional, this does not effect the computational efficiency greatly. The boundary is also extended 3000 meters at each end of the road to diminish the boundary effects.

The triangulation for the GRFs then become

$$\omega_{\mathrm{S}}(s) = \sum_{j=1}^{V} \delta_{j,\mathrm{S}} \varphi_j(s) \quad \text{and} \quad \xi_{t,\mathrm{S}}(s) = \sum_{j=1}^{V} \psi_{j,t,\mathrm{S}} \varphi_j(s), \tag{4.1}$$

following Equation (3.9), where $\delta_{j,\mathrm{S}}$ and $\psi_{j,t,\mathrm{S}}$ are the weights. The triangulation is the same for the GRFs, and thus the basis functions $\{\varphi_1(s), \ldots, \varphi_V(s)\}$ are equal for the GRFs. However, the weights for the different basis functions are different. One can then define a projector matrix, called the A-matrix, as $A \in \mathbb{R}^{n \times V}$ with elements

$$A = \begin{bmatrix} \varphi_1(s_1) & \cdots & \varphi_V(s_1) \\ \vdots & \ddots & \vdots \\ \varphi_1(s_n) & \cdots & \varphi_V(s_n) \end{bmatrix}.$$

The linear predictor can then be expressed as

$$\eta_{t,\mathrm{S}}(s) = \beta_{\mathrm{Ab}} x_{\mathrm{Ab}} + \beta_{\mathrm{Agb}} x_{\mathrm{Agb}} + \beta_{\mathrm{Ska}} x_{\mathrm{Ska}} + \beta_{\mathrm{w}} x_{\mathrm{w}} + \gamma_t + A_i(\boldsymbol{\delta}_{\mathrm{S}} + \boldsymbol{\psi}_{t,\mathrm{S}}), \tag{4.2}$$

where A_i is row i of A, and $\boldsymbol{\delta}_{\mathrm{S}} = (\delta_{1,\mathrm{S}}, \ldots, \delta_{V,\mathrm{S}}) \sim \mathrm{Normal}(\mathbf{0}, Q_{\mathrm{S}})$ and $\boldsymbol{\psi}_{t,\mathrm{S}} = (\psi_{1,t,\mathrm{S}}, \ldots, \psi_{V,t,\mathrm{S}}) \sim \mathrm{Normal}(\mathbf{0}, Q_{\mathrm{S}})$ are column vectors, where Q_{S} is as given in Equation (3.10).

In the spatial stationary case, the hyperparameters controlling the dependence structure of the GRFs are determined by setting priors on the range ρ and standard deviation σ, as specified in Equation (3.8). This allows for easier interpretation of the priors, compared to setting priors on κ and τ in the SPDE in Equation (3.6).

4.3.1 Choosing Priors

The latent Gaussian field can be denoted by $\mathbf{x}_{\mathrm{S}} = (\boldsymbol{\beta}, \boldsymbol{\gamma}, \boldsymbol{\delta}_{\mathrm{S}}, \boldsymbol{\psi}_{\mathrm{S}})$, as the elements are assigned Gaussian priors. The priors for $\boldsymbol{\beta}$, $\boldsymbol{\gamma}$, τ_γ and τ_ε are as in Section 4.2. The difference lies in the priors for the spatial range ρ and the marginal standard deviation σ for the GRFs.

The priors for the GRFs $\omega_{\mathrm{S}}(s)$ and $\xi_{t,\mathrm{S}}(s)$ are set through the spatial range and marginal standard deviation from Equation (3.8) following the penalised complexity (PC) prior framework. The prior for the range is set through the probability $\Pr(\rho < 100) = 0.1$, that is, there is a 10 percent probability that the spatial range is less than 100 meters. Similarly, the prior for the marginal standard deviation is set through the probability $\Pr(\sigma > 2.5) = 0.1$, that is, there is a 10 percent probability that the marginal standard deviation for the rutting is over 2.5 millimeters. These priors are the same for all the spatial fields, and are set through considering the data, especially the rutting in Figure 2.3 and the semivariogram in Figure 2.13.

4.4 Spatial Non-Stationary Model for Rutting

For the spatial non-stationary model the linear predictor takes the form

$$\eta_{t,\mathrm{NS}}(s) = \beta_{\mathrm{Ab}} x_{\mathrm{Ab}} + \beta_{\mathrm{Agb}} x_{\mathrm{Agb}} + \beta_{\mathrm{Ska}} x_{\mathrm{Ska}} + \beta_{\mathrm{w}} x_{\mathrm{w}} + \gamma_t + \omega_{\mathrm{NS}}(s) + \xi_{t,\mathrm{NS}}(s),$$

where the subscript NS symbolises the non-stationarity of the linear predictor and the GRFs. Other than this, there is no difference in the linear predictor, contra the spatial stationary case. The AADT is introduced in the dependence structure for the non-stationary fields $\omega_{\mathrm{NS}}(s)$ and $\xi_{t,\mathrm{NS}}(s)$ for $t = 1, \dots, T$, dependent on the location s. This inclusion of the AADT is consistent with the fixed effects being scaled by the AADT. This non-stationarity is also included in the model, as it would be expected that the marginal standard deviation of the GRFs would change based on the AADT.

The triangulation for the non-stationary GRFs becomes

$$\omega_{\mathrm{NS}}(s) = \sum_{j=1}^{V} \delta_{j,\mathrm{NS}} \varphi_j(s) \quad \text{and} \quad \xi_{t,\mathrm{NS}}(s) = \sum_{j=1}^{V} \psi_{j,t,\mathrm{NS}} \varphi_j(s),$$

where the basis functions are the same as in Equation (4.1), but the weights are different. Now, the linear predictor can be expressed as

$$\eta_{t,\mathrm{NS}}(s) = \beta_{\mathrm{Ab}} x_{\mathrm{Ab}} + \beta_{\mathrm{Agb}} x_{\mathrm{Agb}} + \beta_{\mathrm{Ska}} x_{\mathrm{Ska}} + \beta_{\mathrm{w}} x_{\mathrm{w}} + \gamma_t + A_i(\boldsymbol{\delta}_{\mathrm{NS}} + \boldsymbol{\psi}_{t,\mathrm{NS}}),$$

where A_i is as in Equation (4.2), and $\boldsymbol{\delta}_{\mathrm{NS}} = (\delta_{1,\mathrm{NS}}, \dots, \delta_{V,\mathrm{NS}}) \sim \mathrm{Normal}(\mathbf{0}, Q_{\mathrm{NS}})$ and $\boldsymbol{\psi}_{t,\mathrm{NS}} = (\psi_{1,t,\mathrm{NS}}, \dots, \psi_{V,t,\mathrm{NS}}) \sim \mathrm{Normal}(\mathbf{0}, Q_{\mathrm{NS}})$ are column vectors, where Q_{NS} is as given in Equation (3.12).

The relation to the SPDE parameters in Equation (3.11) is log-linear to the hyperparameters $(\theta_1, \theta_2, \theta_3, \theta_4)$ given by

$$\ln(\tau(s)) = \theta_1 + \theta_2 \mathrm{AADT}(s) \quad \text{and} \quad \ln(\kappa(s)) = \theta_3 + \theta_4 \mathrm{AADT}(s). \tag{4.3}$$

If $\theta_2 = \theta_4 = 0$ we observe that this is equivalent to the stationary case, with a different parameterization than discussed in Section 4.3.

4.4.1 Choosing Priors

The latent Gaussian field is $\mathbf{x}_{\mathrm{NS}} = (\boldsymbol{\beta}, \boldsymbol{\gamma}, \boldsymbol{\delta}_{\mathrm{NS}}, \boldsymbol{\psi}_{\mathrm{NS}})$, and the priors for $\boldsymbol{\beta}$, $\boldsymbol{\gamma}$, τ_γ and τ_ε are as in Section 4.2. The difference lies in the choice for priors for the hyperparameters $(\theta_1, \theta_2, \theta_3, \theta_4)$.

The hyperparameters θ_2 and θ_4 are given $\mathrm{Normal}(0, 1)$ priors, as the prior assumption is that the spatial range and marginal standard deviation has no effect of varying AADT. Further more, the prior for θ_1 and θ_3 are chosen based on the results from the stationary model. Assuming no effect of varying AADT, $\ln(\tau(s)) = \theta_1$ and $\ln(\kappa(s)) = \theta_3$, such that, using Equation (3.8),

$$\theta_1 \approx -\ln(2) - \ln(\sigma) - \frac{3}{2}\theta_3 \quad \text{and} \quad \theta_3 \approx \ln(2\sqrt{3}) - \ln(\rho).$$

Using the mean of the range and the mean of the marginal standard deviations for the spatial fields obtained for the stationary model we set the mean of the priors for θ_1 and θ_3. The precision for the priors are set to one, to allow flexibility in the model. Thus, the priors are $\theta_1 \sim \mathrm{Normal}(7.805, 1)$ and $\theta_3 \sim \mathrm{Normal}(-5.665, 1)$.

4.5 Inference, Prediction, and the Software

The non-spatial model is fitted using a Bayesian linear regression over the covariates. The spatial models for the rutting fit into the latent Gaussian model framework, as the elements of $\mathbf{x}_{\mathrm{S}}$ and $\mathbf{x}_{\mathrm{NS}}$ are assumed to have Gaussian priors. The spatial effects $\omega_{\mathrm{S}}(s)$, $\xi_{t,\mathrm{S}}(s)$, $\omega_{\mathrm{NS}}(s)$, and $\xi_{t,\mathrm{NS}}(s)$ are modeled as Gaussian random fields, and together with the stochastic partial differential equation approach to spatial modeling, a Gaussian Markov random field representation is obtained. This makes integrated nested Laplace approximations applicable for fast approximate Bayesian inference. The data analysis is performed in `R` (R Core Team, 2020), whilst the INLA framework implemented in `R-INLA` (Rue, Martino and Chopin, 2009) is used for fast inference and prediction.

Most plotting is done using `ggplot2` (Wickham, 2016), however the different map plots are generated through `mapview` (Appelhans et al., 2022). In addition to this, `gstat` (Gräler, Pebesma and Heuvelink, 2016; Pebesma, 2004) is used for the different variogram plots. The package `sf` (Pebesma, 2018) is used for handling the spatial properties of the data.

The `R` code and publicly available data from this thesis can be found on GitHub https://github.com/wsolsen/TMA4900-MasterThesis-SMARTerMaintenance.

CHAPTER 5

Results for the Rutting

In this chapter the results for the non-spatial, the spatial stationary, and the spatial non-stationary models for the rutting described in Chapter 4 are presented. Results for the fixed effects, random yearly effect, and residuals are first presented for the spatial non-stationary model, and then the estimates for these variables are compared between the three models. Then the spatial effects are presented for the spatial non-stationary model. This is then compared to the results from the spatial stationary model based on how well they fit the data, and also a comparison of the stationary and non-stationary assumptions. This chapter concludes with a practical application of the inferred results for predicting the rutting along a stretch of European route E16 between Bergen and Voss forward in time.

5.1 Fixed Effects, Random Yearly Effect, and Residuals

This section starts with a presentation of the estimated parameters of the fixed effects, the random yearly effect, and the residuals for the spatial non-stationary model for the rutting. Then a comparison of these estimated parameters are done with those estimated from the spatial stationary model, and the non-spatial model for the rutting.

5.1.1 Spatial Non-Stationary Model for Rutting

The estimates for the parameters of the fixed effects from the spatial non-stationary model for the rutting is shown in Figure 5.1 as a function of the AADT. These results show that the use of road cover type asphalt gravel concrete leads to the most expected rutting, while asphalt concrete gives the least expected rutting, closely followed by stone mastic asphalt. These are the expected results following the NPRA. A selection of road widths are plotted between 3.5 meters and 6.5 meters. Then it is clear that for an increase in the road width, the expected rutting decreases, also to be expected from earlier discussions. Assuming a road width of five meters, the total expected rutting from the fixed effect for each road cover type is plotted in Figure 5.2. This shows that even though the expected rutting was negative in Figure 5.1b, the total effect of the fixed effects will always be positive. Also the expected rutting will always increase with an increase in the AADT.

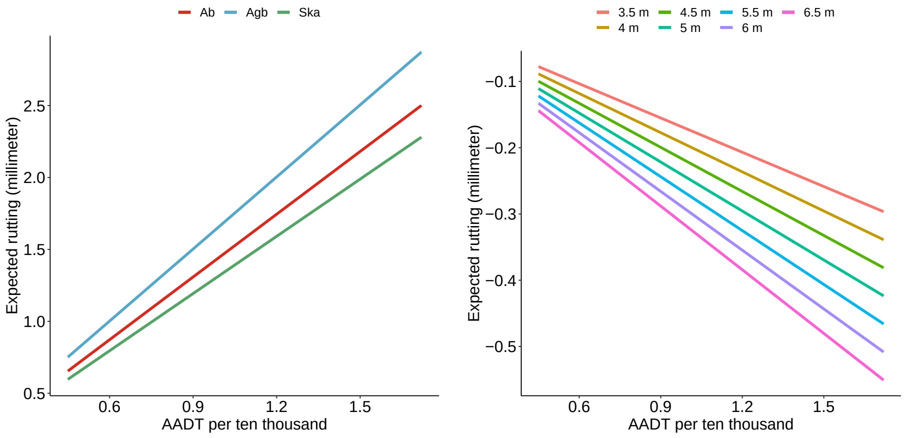

(a) The road cover type. (b) The road width.

Figure 5.1: The fixed effect of the road cover type and the road width for the spatial non-stationary model for the rutting as a function of the AADT.

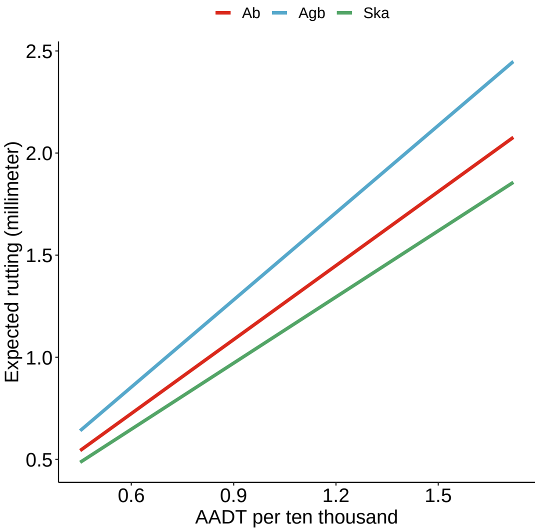

Figure 5.2: The total expected rutting from the fixed effects for each road cover type as a function of the AADT, assuming a road width of 5 meters, for the spatial non-stationary model for the rutting.

Parameter	Mean/Median	95% credible interval
β_{Ab}	1.454	$[1.343, 1.565]$
β_{Agb}	1.670	$[1.481, 1.859]$
β_{Ska}	1.326	$[1.081, 1.571]$
β_{w}	-0.049	$[-0.078, -0.020]$
σ_γ	0.297	$[0.206, 0.460]$
σ_ε	0.887	$[0.877, 0.894]$

Table 5.1: The parameter estimates for the spatial non-stationary model for the rutting with a 95% credible interval. The median is reported for σ_γ and σ_ε, and the mean for the rest of the parameters.

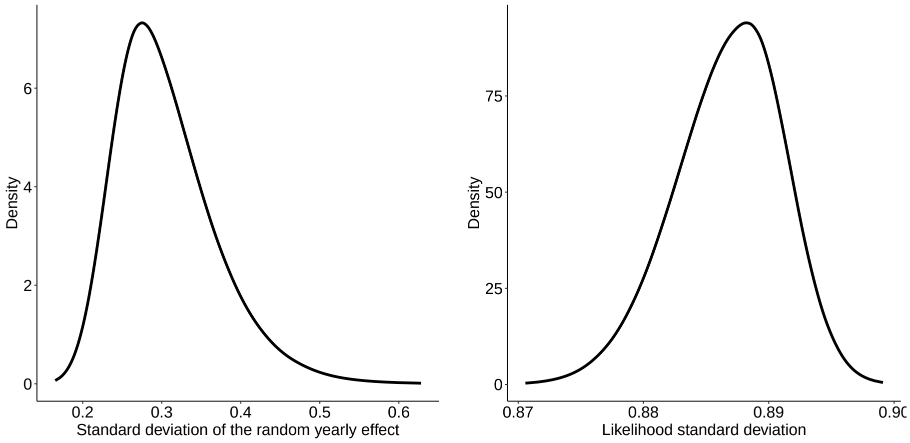

(a) For the yearly effect.

(b) For the Gaussian observations.

Figure 5.3: The posterior marginal distribution for the standard deviation of the random yearly effect and the residuals for the spatial non-stationary model for the rutting.

The parameter estimates for the fixed effects and the standard deviation for the yearly random effect and the residuals for the spatial non-stationary model for the rutting is shown in Table 5.1 with a 95% credible interval. At this level, none of the 95% credible intervals contains zero. The estimated median of the standard deviation of the yearly effect is 0.297 millimeter, and the posterior marginal distribution of this is shown in Figure 5.3a. This shows evidence of being some difference in the rutting between the years. However, the 95% credible interval is quite wide, meaning that there is considerable uncertainty in the standard deviation coming from the yearly effect. The estimated median of the standard deviation of the residuals are 0.887 millimeter, and the posterior marginal distribution of this is shown in Figure 5.3b. This is the standard deviation in the model not explained by other factors, and the 95% credible interval is quite narrow, making this estimate less uncertain. Thus, there is quite a lot of unexplained variance in the residuals.

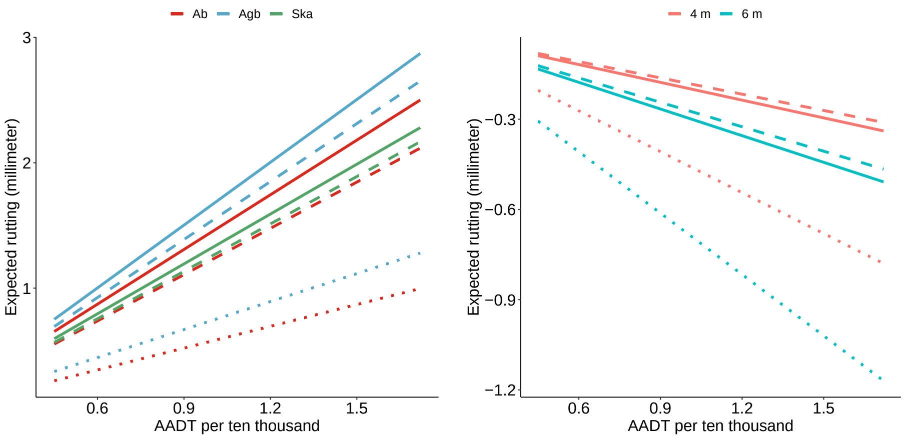

(a) The road cover type.

(b) The road width.

Figure 5.4: The fixed effect of the road cover type and the road width for the spatial non-stationary model in drawn lines, for the spatial stationary model in dashed lines, and for the non-spatial model in dotted lines, all as a function of the AADT.

5.1.2 Comparing With Non-Spatial and Spatial Stationary Model for Rutting

Figure 5.4 shows the estimates for the parameters of the fixed effects for the three proposed models as a function of the AADT. The estimates for the spatial non-stationary model are shown as drawn lines, the estimates for the spatial stationary model are shown as dashed lines, and the estimates for the non-spatial model are shown as dotted lines. The results for road cover type stone mastic asphalt is not included for the non-spatial model, and a discussion of this is given later in this section.

From Figure 5.4a there are large similarities between the spatial stationary and non-stationary models, compared to the non-spatial model. However, the trend seems to be similar, for which road cover type asphalt gravel concrete gives a higher expected rutting. For the spatial stationary model, the expected rutting for the road cover types asphalt concrete and stone mastic asphalt are quite similar, which is different from the spatial non-stationary model.

Figure 5.4b shows the expected rutting based on different road widths, here 4 meters and 6 meters. For all three models the results are that the expected rutting decreases with an increase in road width. The difference between the expected rutting for each road width also increases with the AADT. The expected rutting is much smaller for the non-spatial model compared to the two spatial models, this indicates that the effect of wider roads is greater for the non-spatial model compared to the two spatial models. A possible explanation for this is that this effect gets incorporated in the spatial properties of the road for the spatial models.

Assuming a road width of five meters, the total expected rutting from the fixed effects for each road cover type is shown in Figure 5.5, where the line

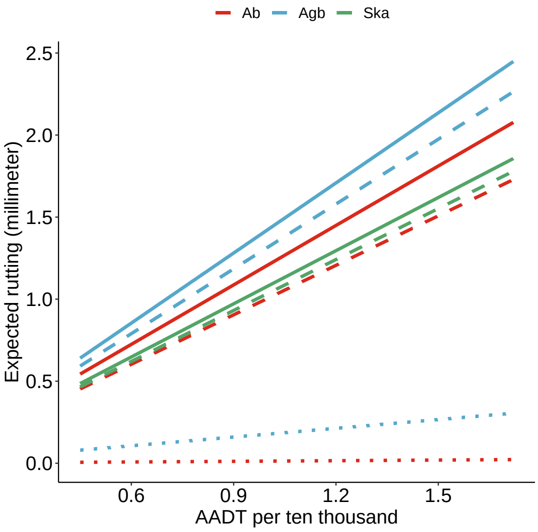

Figure 5.5: The total expected rutting from the fixed effects for each road cover type as a function of the AADT, assuming a road width of 5 meters for the spatial non-stationary model in drawn lines, the spatial stationary model in dashed lines, and the non-spatial model in dotted lines.

types describe the same model as in Figure 5.4. For the non-spatial model the effects on the rutting is negligible for road cover type asphalt concrete, and there is only a small increase for road cover asphalt gravel concrete based on the AADT. For the two spatial models, the trend is similar, with an increase in the expected rutting when the AADT increases. The expected rutting is also always positive for these two models, despite the negative expected rutting in Figure 5.4b.

The parameter estimates for the fixed effects, and the standard deviation for the yearly random effect and the residuals for the non-spatial model is shown in Table 5.2. None of the 95% credible intervals contains zero. Comparing to the parameter estimates for the spatial non-stationary model in Table 5.1 confirms what Figure 5.4 shows. Looking at the estimate of β_{Ska} shows that the reason it is not included in Figure 5.4 and Figure 5.5 is because it is negative, and would impact the scaling on the axis making comparison of the other models more difficult. For road cover type stone mastic asphalt the expected rutting is then decreasing for increasing values of the AADT. This may follow from the fact that there is little variability of AADT values for this road cover type, as seen in Figure 2.12. In fact, most part of the road stretch having road cover type stone mastic asphalt has an AADT of 4500, while some small parts have an AADT of 4649 or 4892. This means that the interaction effect x_{Ska} is mainly just an effect of the road cover type, and not the interaction. This then indicates that using road cover type stone mastic asphalt leads to lower rutting than using the other two road cover types.

Similarly, the parameter estimates for the fixed effects, and the standard deviation for the yearly random effect and the residuals for the spatial stationary

Parameter	Mean/Median	95% credible interval
β_{Ab}	0.580	$[0.533, 0.627]$
β_{Agb}	0.744	$[0.657, 0.831]$
β_{Ska}	-0.202	$[-0.338, -0.065]$
β_{w}	-0.113	$[-0.125, -0.102]$
σ_γ	0.971	$[0.584, 1.835]$
σ_ε	0.985	$[0.971, 0.996]$

Table 5.2: The posterior parameter estimates for the non-spatial model for the rutting with a 95% credible interval. The median is reported for σ_γ and σ_ε, and the mean for the rest of the parameters.

Parameter	Mean/Median	95% credible interval
β_{Ab}	1.231	$[1.115, 1.347]$
β_{Agb}	1.542	$[1.321, 1.763]$
β_{Ska}	1.260	$[0.918, 1.602]$
β_{w}	-0.045	$[-0.077, -0.014]$
σ_γ	0.455	$[0.251, 0.861]$
σ_ε	0.886	$[0.878, 0.894]$

Table 5.3: The posterior parameter estimates for the spatial stationary model for the rutting with a 95% credible interval. The median is reported for σ_γ and σ_ε, and the mean for the rest of the parameters.

model is shown in Table 5.2. None of the 95% credible intervals contains zero. This table, compared to that of the spatial non-stationary model in Table 5.1 shows quite similar results.

The posterior marginal distribution for the standard deviation of the random yearly effect and the residuals for the non-spatial model, the spatial stationary model, and the spatial non-stationary model for the rutting is shown in Figure 5.6. The posterior marginal distribution for the standard deviation of the random yearly effect for each of the models have a quite different form, as shown in Figure 5.6a. The yearly effect is greatest for the non-spatial model, and it also has the widest 95% credible interval, as confirmed by Table 5.2. This means that there is greatest difference in the expected rutting between the years for this model. Some of the yearly effect can be incorporated in the spatial effect instead, resulting in a lower yearly effect for the spatial stationary effect. The 95% credible interval, as shown in Table 5.3 is still quite wide, giving some uncertainty of the yearly effect. The random yearly effect for the spatial non-stationary effect is the smallest, and least uncertain. A reason for this may be that this effect is better captured in the non-stationary spatial fields.

The posterior marginal distribution for the standard deviation of the residuals is shown in Figure 5.6b. This is the distribution of the standard deviation in the models not explained by other factors. It is then clear that both the spatial stationary and non-stationary models have approximately the same amount of unexplained standard deviation. The unexplained standard deviation for the non-spatial model is much larger than for the other two models. This is

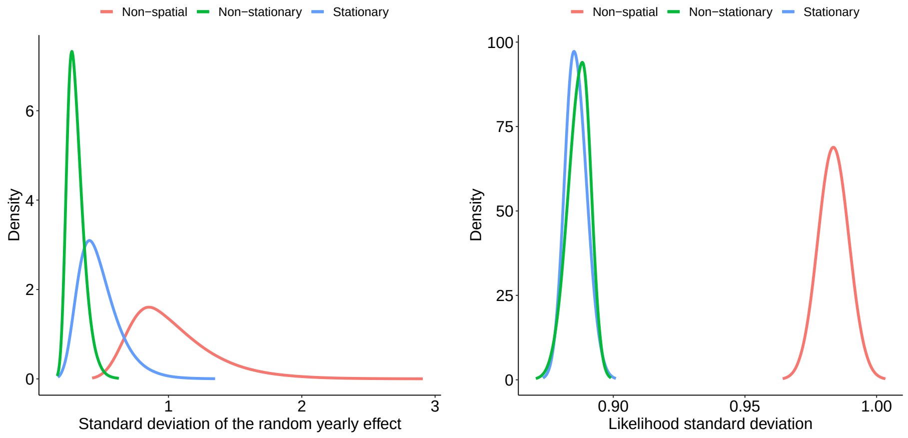

(a) For the yearly effect. (b) For the Gaussian observations.

Figure 5.6: The posterior marginal distribution for the standard deviation of the random yearly effect and the residuals for the non-spatial model, the spatial stationary model, and the spatial non-stationary model for the rutting.

an indication that the spatial properties included in the spatial stationary and non-stationary models explain more of the otherwise unexplained variance.

5.2 Spatial Effects

This section first introduces the results for the spatial fields for the spatial non-stationary model. Then a comparison of these results are done with those of the spatial stationary model. A discussion of using sum-to-zero constraints on the spatial fields is given in Appendix C, and this is not done for the spatial fields presented here.

5.2.1 Spatial Non-Stationary Model for Rutting

The posterior mean of the rutting from the common spatial field $\omega_{\text{NS}}(s)$ for the spatial non-stationary model with a 95% credible interval and on the map between Bergen and Voss is shown in Figure 5.7. The interpretation of this is that it is the difference from the expected rutting from each road segment if there were no spatial effect. It is then clear that close to Bergen the rutting is lower than expected, but it increases towards Voss, and near Voss the rutting is progressively worse than expected. There are also some spikes in both positive and negative directions for some road segments, but the trend is that the rutting gets progressively worse than expected from Bergen moving towards Voss.

The posterior mean of the rutting from the annually varying spatial field $\xi_{t,\text{NS}}(s)$ for the years 2017 to 2020 is shown in Figure 5.8. This describes the annual spatial deviation from the spatial field $\omega_{\text{NS}}(s)$ for each of the years from 2017 to 2020. From the figures it is clear that there is a great difference between the different years. For the year 2017 it seams that there was less expected rutting close to Bergen, and increasing towards Voss. This also holds for the

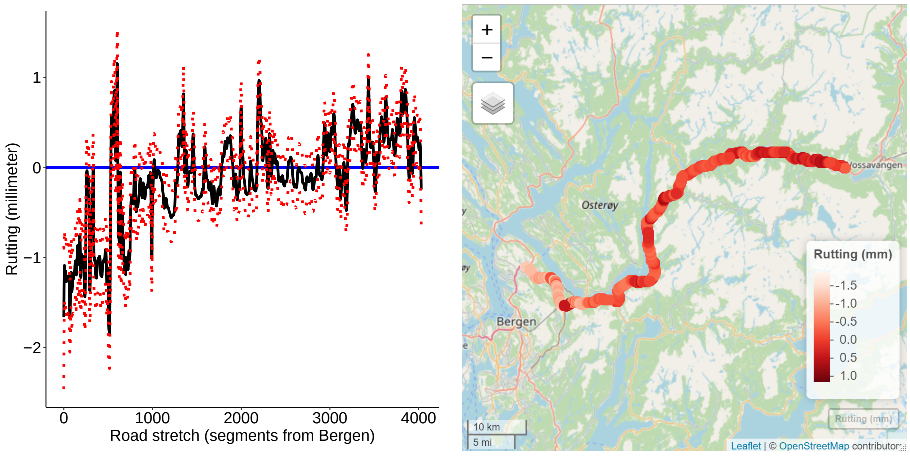

(a) With a 95% credible interval.

(b) On the map.

Figure 5.7: The rutting inferred from the common spatial field $\omega_{\mathrm{NS}}(s)$ for the non-stationary model with a 95% credible interval and on the map between Bergen and Voss.

year 2018, and for both these years, the results fluctuates between positive and negative values for the rutting. For the year 2019 there was more than the expected rutting for almost all of the road, that is, the results were positive. This can be explained by there being higher rutting in the year 2019 compared to the other ones, as seen in Figure 2.3. The year 2020 is more similar again to the years 2017 and 2018, with more fluctuation between positive and negative values.

The estimates for the parameters $(\theta_1, \theta_2, \theta_3, \theta_4)$ governing the spatial fields are given in Table B.2 in Appendix B with 95% credible intervals. From this set of parameters the spatial range and marginal standard deviation for the spatial fields can be computed as a function of the AADT using Equation (4.3) and Equation (3.13). This gives the result in Figure 5.9, where the spatial range and marginal standard deviation are plotted as a function of the AADT for the different spatial fields. From this there is evidence of non-stationarity for all the spatial fields, with some being more prominent than others. For the years 2017, 2018 and 2020 we see that the spatial range increases as the AADT increases, while for the time constant common field and for year 2019 we see a decrease of the spatial range. Similarly for the years 2018 and 2020, in addition to for the time constant common field, the marginal standard deviation increases with the AADT, while for the years 2017 and 2019 we see a decrease in the marginal standard deviation.

5.2.2 Comparing With Spatial Stationary Model for Rutting

In this section the spatial effects for the spatial non-stationary model is compared to those for the spatial stationary model. The posterior mean of the rutting from the common spatial field $\omega_{\mathrm{S}}(s)$ for the stationary model with a 95% credible interval and on the map between Bergen and Voss is shown in Figure 5.10.

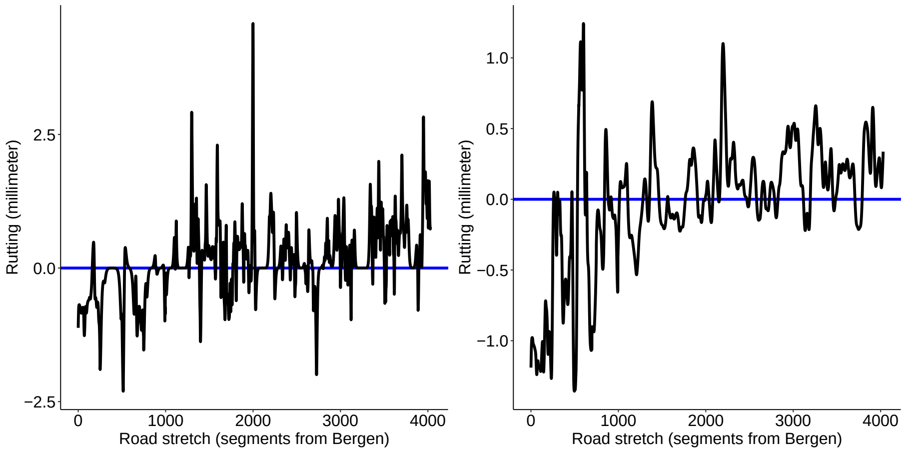

(a) For the year 2017.

(b) For the year 2018.

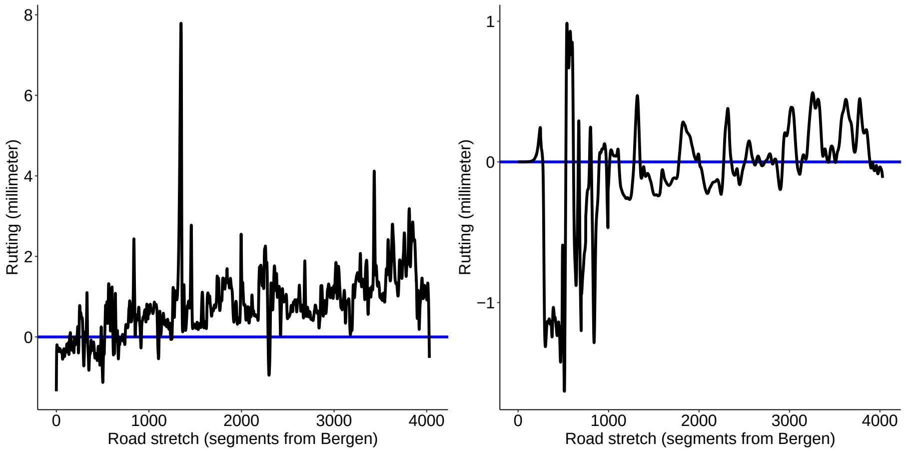

(c) For the year 2019.

(d) For the year 2020.

Figure 5.8: The annual spatial deviation from the spatial field $\omega_{\text{NS}}(s)$ for each of the years from 2017 to 2020.

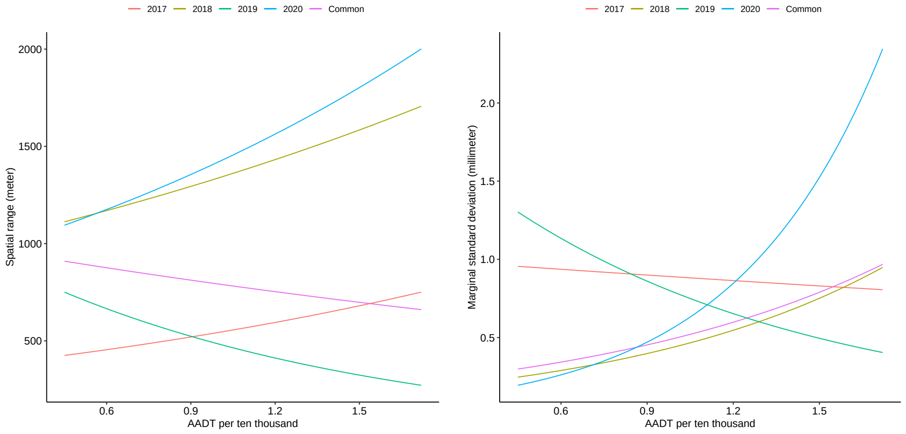

(a) The spatial range. (b) The marginal standard deviation.

Figure 5.9: The spatial range and marginal standard deviation for the spatial fields from the spatial non-stationary model as a function of the AADT.

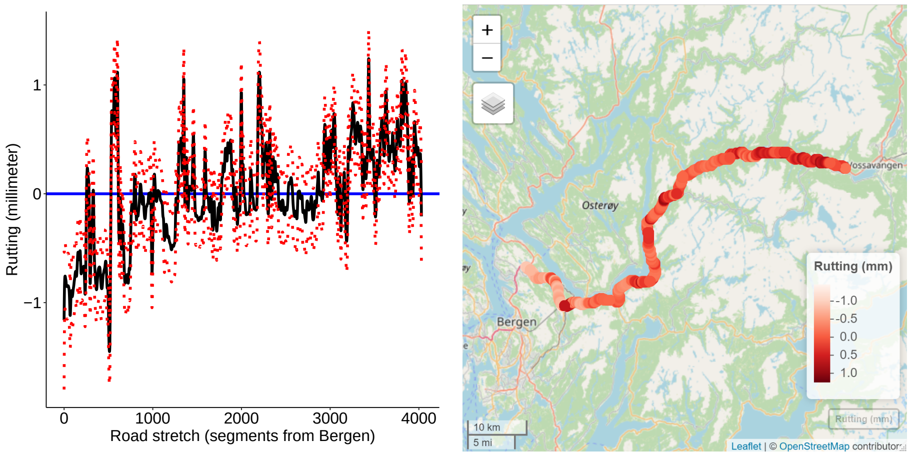

(a) With a 95% credible interval. (b) On the map.

Figure 5.10: The posterior mean of the rutting from the common spatial field $\omega_{\mathrm{S}}(s)$ for the spatial stationary model with a 95% credible interval and on the map between Bergen and Voss.

Again, the rutting closer to Bergen is lower than expected, but increases towards Voss. Figure 5.11 shows the posterior mean of the rutting from the common spatial field $\omega_{\mathrm{NS}}(s)$ for the spatial non-stationary model in drawn red, and from the common spatial field $\omega_{\mathrm{S}}(s)$ for the spatial stationary model in dashed blue. The posterior means for the two models are quite similar, and shows the same trends for both the spatial non-stationary model and the spatial stationary model.

Similarly, Figure 5.12 shows the annual spatial deviation from the spatial

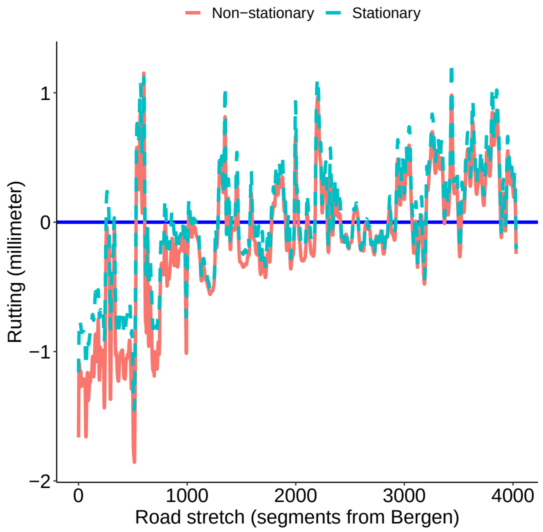

Figure 5.11: The posterior mean of the rutting from the common spatial field $\omega_{\text{NS}}(s)$ for the spatial non-stationary model in drawn red, and from the common spatial field $\omega_{\text{S}}(s)$ for the spatial stationary model in dashed blue.

field $\omega_{\text{NS}}(s)$ for each of the years from 2017 to 2020 in drawn red, and from $\omega_{\text{S}}(s)$ for each of the years from 2017 to 2020 in dashed blue. Here as well the results are quite similar, especially in the trends that were discussed in Section 5.2.1.

The estimates of the spatial range parameters and marginal standard deviation parameters governing the spatial fields for the spatial stationary model are given in Table B.1 in Appendix B with a 95% credible interval. Figure 5.13 shows the spatial range and marginal standard deviation for the spatial fields from the spatial non-stationary model as drawn lines, and from the spatial stationary model as dashed lines, as a function of the AADT. This shows that the values of the spatial range and marginal standard deviation for the spatial non-stationary model are different from those for the spatial stationary model. There is also a clear evidence of spatial non-stationarity, as discussed in Section 5.2.1.

5.3 Comparison of the Models

Different values for model selection criteria for the non-spatial model, the spatial stationary model, and the spatial non-stationary model is presented in Table 5.4. As discussed in Section 3.7, smaller DIC and WAIC are preferred, while a larger marginal log-likelihood is preferred. From this table alone, the non-spatial model is preferred. However, from our previous discussions it seems that it is reasonable to include spatial fields, as they seem to explain more of the otherwise unexplained variance. Including spatial fields also give more interpretative results regarding the expected rutting based on the road cover types. The discussion around Figure 5.9 points to there being a non-stationary

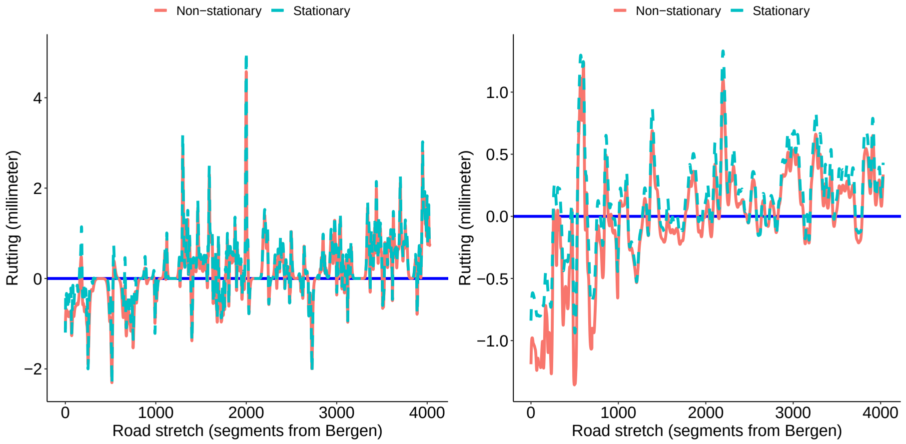

(a) For the year 2017.

(b) For the year 2018.

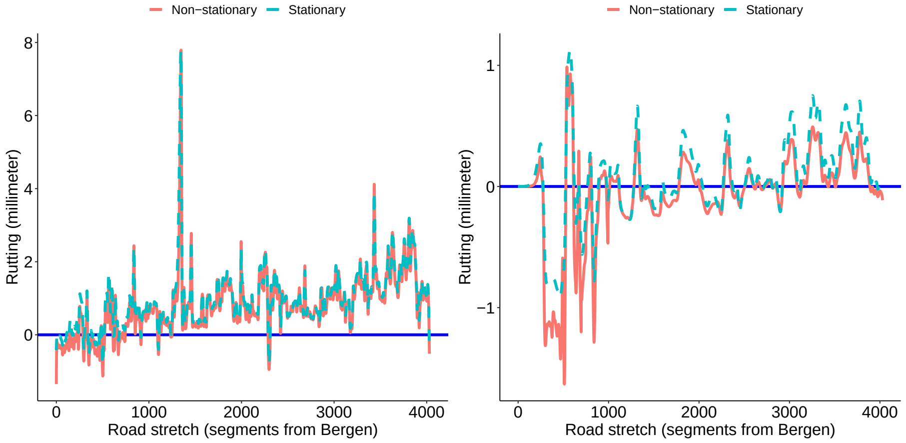

(c) For the year 2019.

(d) For the year 2020.

Figure 5.12: The annual spatial deviation from the spatial field $\omega_{\text{NS}}(s)$ for each of the years from 2017 to 2020 in drawn red, and from $\omega_{\text{S}}(s)$ for each of the years from 2017 to 2020 in dashed blue.

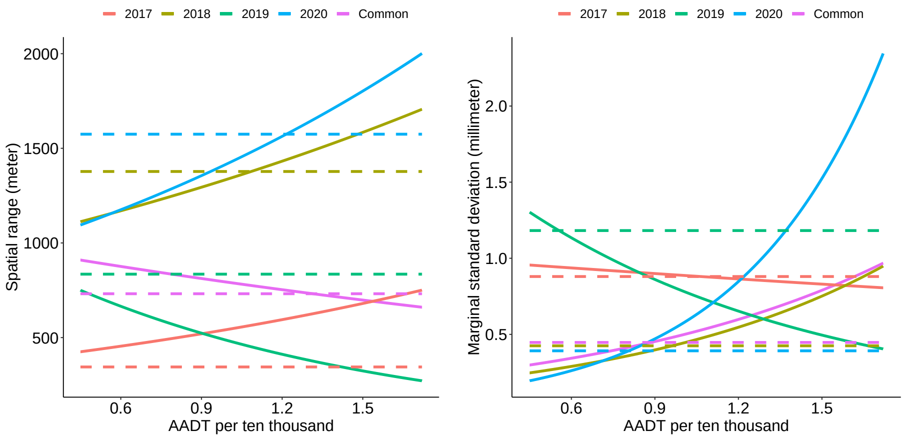

(a) The spatial range. (b) The marginal standard deviation.

Figure 5.13: The spatial range and marginal standard deviation for the spatial fields from the spatial non-stationary model as drawn lines, and from the spatial stationary model as dashed lines, as a function of the AADT.

	Non-spatial	Stationary	Non-stationary
DIC	38737.37	66951.93	66451.67
WAIC	37000.46	104288.39	144519.11
Marginal log-likelihood	−19430.25	−37250.85	−37196.46

Table 5.4: Model assessment criteria for the model with no spatial effects, the spatial stationary model, and the spatial non-stationary model.

effect of the AADT for the spatial fields. For this reason, the non-stationary model is the prefered model, and we will create predictions using this model in the next section.

5.4 Prediction With Uncertainty

When doing prediction through `R-INLA`, it is the posterior distribution of η_{NS} that is predicted. This has the same expected value as the rutting, and we therefore use the term predicted rutting. The predicted[1] rutting for year 2021 for the European route E16 between Bergen and Voss is shown in Figure 5.14 with a 95% credible interval, and on the map between Bergen and Voss. The predicted 95% credible interval is the credible interval for η_{NS}, and if the predictions were to be compared to the data for 2021, the uncertainty in the residuals would also need to be included. The prediction is done using the spatial non-stationary model for rutting. From this the predicted rutting is largest close to Bergen, where the AADT is the highest. Here the rutting lies around 2 millimeters, which in only 10 years would give a rut depth of about 20

---

[1] Even though this thesis is published in the year 2022, the data for the rut depth in year 2021 was not available at the time of writing.

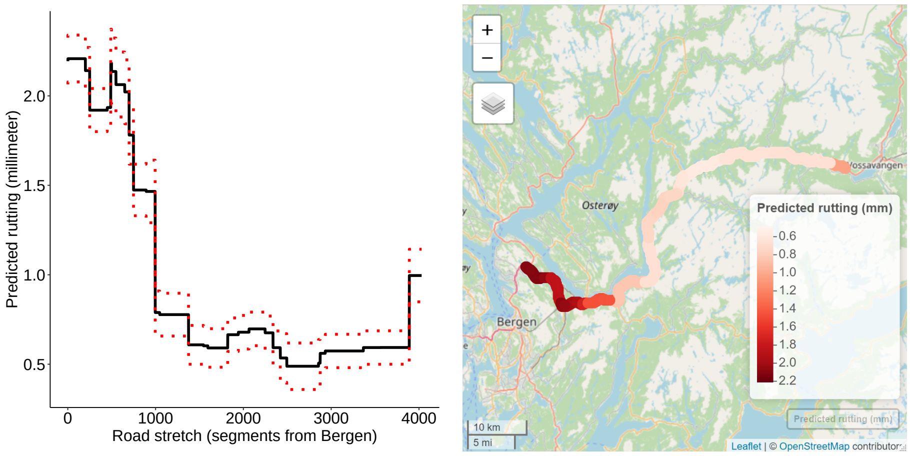

(a) With a 95% credible interval.

(b) On the map.

Figure 5.14: The predicted rutting for year 2021 with a 95% credible interval, and on the map between Bergen and Voss.

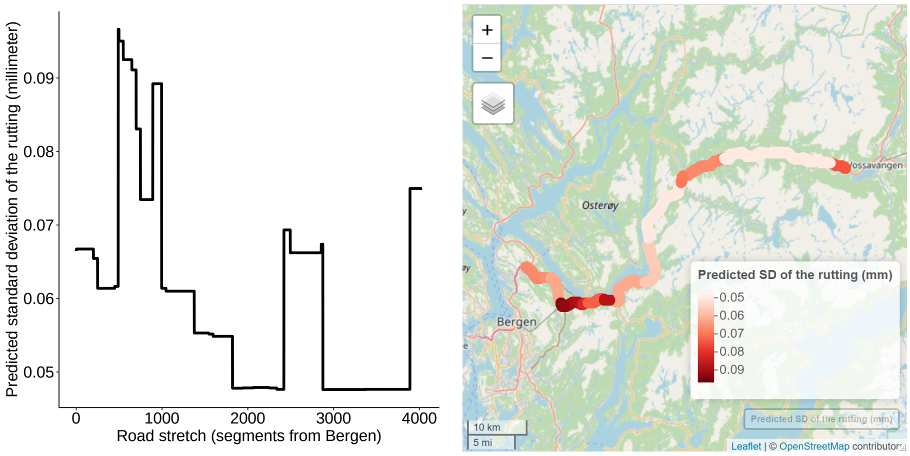

(a) For each road segment.

(b) On the map.

Figure 5.15: The predicted standard deviation of the rutting for year 2021 for each road segment, and on the map between Bergen and Voss.

millimeters, prompting a repaving. We can also see that the predicted rutting decreases towards Voss, which is to be expected as the AADT decreases in this direction.

The predicted standard deviation of the rutting for the European route E16 between Bergen and Voss is shown in Figure 5.15, which we see lies beneath 0.1 millimeter for the whole road stretch. A 95% credible interval for the predicted rutting is also shown in Figure 5.14a, which also confirms that the prediction is quite certain. The predicted standard deviation fluctuates, but in general it is larger where AADT is higher.

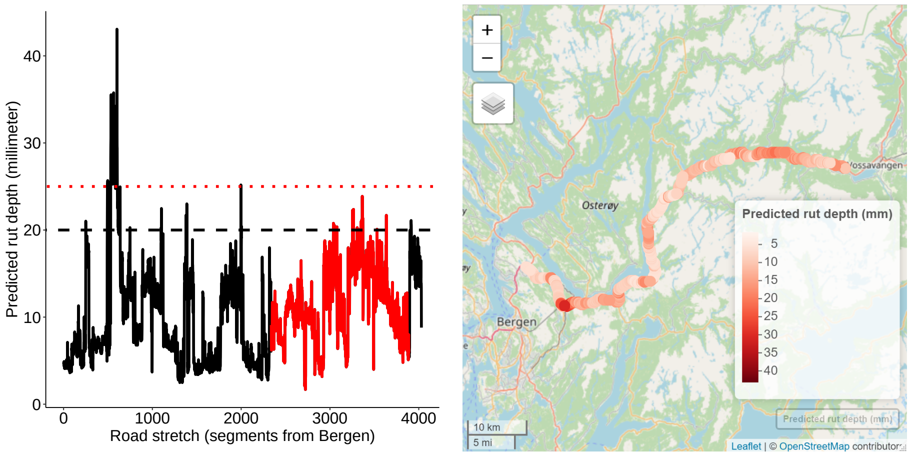

(a) For each road segment.

(b) On the map.

Figure 5.16: The predicted rut depth for year 2021 for each road segment, and on the map between Bergen and Voss. The road colored red on the right hand side is that which has an AADT of less than 5000, while the road colored black has an AADT of higher than 5000. A dotted red line is drawn at 25 millimeters of predicted rutting, while a dashed black line is drawn at 20 millimeters of predicted rutting.

Figure 5.16 shows the predicted rut depth for the European route E16 between Bergen and Voss for the year 2021, which is found by adding the predicted rutting for 2021 to the rut depth from year 2020. In Figure 5.16a the road stretch coloured in black has an AADT of more than 5000, while the road stretch coloured in red has an AADT of less than 5000. The maximum allowed rut depth for roads with an AADT of above 5000 is 20 millimeters, while it is 25 millimeters for roads with an AADT of less than 5000 (Norwegian Public Roads Administration, 2014). The part of the road colored red has to stay below the upper dotted red line, which we see that it indeed does. Some of the road segments, however, starts to reach a rut depth in which repaving is needed. For the rest of the road, it is the lower dashed black line which is the threshold for the rut depth. We then see that there are some single spikes above the threshold, however, many of these are only small stretches of road. There is also a larger and wider spike, upwards of a rut depth of 40 millimeters. This is well over the allowed rut depth, and has to be repaved.

A prediction of the rut depth for the 200 first road segments from Bergen approaching Voss is shown with a 95% credible interval in Figure 5.17. This constitutes 4 kilometers of road, and we see that the credible interval lies close to the predicted mean.

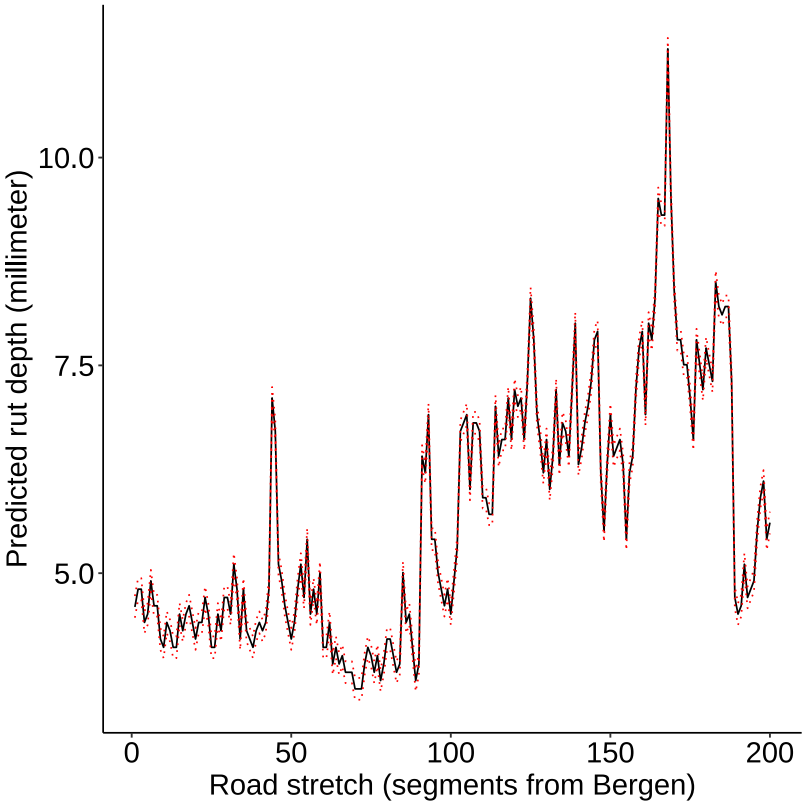

Figure 5.17: The predicted rut depth with a 95% credible interval for the 200 first road segments from Bergen approaching Voss.

CHAPTER 6

Discussion, Final Remarks, and Further Work

In this thesis we investigated the rutting along the European route E16 between Bergen and Voss with an aim to identify factors responsible for increased rutting, and to investigate whether spatial dependencies between road segments impacts the rutting. In this chapter the main results are summarised before some suggestions for further work is presented.

The proposed spatial non-stationary model is the preferred model based on our analysis. We found that spatial effects improved the interpretability of the model, and because of the way a road is constructed, spatial effects are to be expected. Results also showed that including the AADT in the dependence structure of the spatial fields seemed to improve the model. The spatial non-stationary model was therefore chosen for inference and prediction. The Gaussian random fields modeling the spatial effects are very prior sensitive, so a more thorough analysis of how to choose the priors should be conducted, and this is a weak point of choosing one of the spatial models. The proposed spatial models should be tested more by the Norwegian Public Roads Administration before they are put to use.

The results for the spatial non-stationary model was that none of the 95% credible intervals for the fixed effects contained zero. The expected rutting was highest for road cover type asphalt gravel concrete, as expected, and road cover type stone mastic asphalt gave the lowest expected rutting. Also according to expectation, the expected rutting decreases with an increase in road width, and the expected rutting increases with an increase in the AADT.

This is also the model in which the random yearly effect explains the least amount of variance, as the spatial non-stationary fields are able to capture this. This also holds for the residual standard deviation, which is lowest for the spatial non-stationary model. This means that the spatial non-stationary model has less unexplained variance than the other two models.

The time constant common spatial field for the non-stationary model shows the difference from the annual expected rutting from each road segment if there were no spatial effect. Close to Bergen this effect is negative, so the expectation is less rutting here, while it increases to positive values close to Voss, where a higher rutting is expected.

A prediction is done for the rutting for year 2021, for which rutting data is not available to us, for the European route E16 between Bergen and Voss with uncertainty. This predicts highest rutting close to Bergen, of about 2 millimeters, and a decrease towards Voss of between 0.5 and 1 millimeter. Using this together with the rut dept data from 2020, the expected rut depth in 2021 can be predicted. This prediction allows us to locate areas in need of repaving, and one such road stretch close to Bergen is found with a rut depth of up to 40 millimeters.

For a more precise prediction, where more of the unexplained variance can be explained, other covariates should also be included in the models. These include for example the pavement age, the proportion of heavy vehicles, the use of studded tires, and climate effects. The spatial non-stationary model requires four hyperparameters per spatial field, so including more year specific spatial fields here would increase the computation time drastically, where the amount of hyperparameters already is large.

Appendices

APPENDIX A

Approximation of the Posterior Marginals in INLA

In this appendix the approximation of the posterior marginals for the hyperparameters and the latent field in INLA is presented, building on the theory presented in Section 3.5. The Gaussian approximation of the full conditional of $\mathbf{x} \mid \mathbf{y}, \boldsymbol{\theta}$ and $\mathbf{x}_{-i} \mid x_i, \boldsymbol{\theta}, \mathbf{y}$ are included for the sake of completeness, and need not be approximated in this theses as the full conditionals already are Gaussian. This is based on the preliminary work by Olsen (2021), and also Martino and Riebler (2019); Rue, Martino and Chopin (2009).

A.1 Approximation of the Posterior Marginals for the Hyperparameters

Approximating the posterior marginals for the hyperparameters is based on the approximation

$$p(\boldsymbol{\theta} \mid \mathbf{y}) \underset{\sim}{\propto} \left. \frac{p(\mathbf{y} \mid \mathbf{x}, \boldsymbol{\theta}) p(\mathbf{x} \mid \boldsymbol{\theta}) p(\boldsymbol{\theta})}{\tilde{p}_{\mathrm{G}}(\mathbf{x} \mid \mathbf{y}, \boldsymbol{\theta})} \right|_{\mathbf{x}=\mathbf{x}^*(\boldsymbol{\theta})}. \tag{A.1}$$

Here we denote by $\tilde{p}_{\mathrm{G}}(\mathbf{x} \mid \mathbf{y}, \boldsymbol{\theta})$, the Gaussian approximation of the full conditional of $\mathbf{x} \mid \mathbf{y}, \boldsymbol{\theta}$ constructed using the Laplace approximation in Section 3.4. If the full conditional of $\mathbf{x} \mid \mathbf{y}, \boldsymbol{\theta}$ already is Gaussian, the Gaussian approximation need not be done, which is the case in this thesis. The mode is denoted $\mathbf{x}^*(\boldsymbol{\theta})$ denotes the mode, and the approximation in Equation (A.1) is denoted by $\tilde{p}(\boldsymbol{\theta} \mid \mathbf{y})$.

As it is computationally costly to evaluate $\tilde{p}(\boldsymbol{\theta} \mid \mathbf{y})$ for a large number of configurations, the integral in Equation (3.4) is computed using suitable integration points $\{\boldsymbol{\theta}^{(k)}\}$. These integration points are found using the following method:

1. Use a quasi-Newton method to optmimize $\ln(\tilde{p}(\boldsymbol{\theta} \mid \mathbf{y}))$ giving $\boldsymbol{\theta}^*$ as the mode of $\tilde{p}(\boldsymbol{\theta} \mid \mathbf{y})$.
2. Compute the negative Hessian[1] H at the modal configuration.

---

[1] The Hessian matrix of a function $f\colon \mathbb{R}^n \to \mathbb{R}$ is defined as having entries $\partial^2 f / \partial x_i \partial x_j$ for $i, j = 1, \ldots, n$. The negative Hessian is also often called the observed Fisher information.

3. Compute the eigen-decomposition $\Sigma = H^{-1} = V\Lambda V^{\top}$, where Σ is the covariance matrix of $\boldsymbol{\theta}$ if it was Gaussian.
4. Define the standardized variable $\mathbf{z}$ by $\boldsymbol{\theta}(\mathbf{z}) = \boldsymbol{\theta}^* + V\Lambda^{1/2}\mathbf{z}$.
5. Find the bulk of the probability mass of $\ln(\tilde{p}(\boldsymbol{\theta} \mid \mathbf{y}))$ using the $\mathbf{z}$-parameterization giving the integration points $\{\boldsymbol{\theta}^{(k)}\}$.

Each posterior marginal $\tilde{p}(\theta_j \mid \mathbf{y})$ in Equation (3.4) can then be found using interpolation on $\tilde{p}(\boldsymbol{\theta} \mid \mathbf{y})$ using the integration points $\{\boldsymbol{\theta}^{(k)}\}$.

A.2 Approximation of the Posterior Marginals for the Latent Field

The approach for finding an approximation of the posterior marginals for the latent field is similar to the method in Appendix A.1. Letting $\mathbf{x} = (x_i, \mathbf{x}_{-i})$, the approximation we denote by $\tilde{p}(x_i, \boldsymbol{\theta} \mid \mathbf{y})$ is found by

$$p(x_i \mid \boldsymbol{\theta}, \mathbf{y}) \propto \frac{p((x_i, \mathbf{x}_{-i}) \mid \boldsymbol{\theta}, \mathbf{y})}{p(\mathbf{x}_{-i} \mid x_i, \boldsymbol{\theta}, \mathbf{y})} \approx \left. \frac{p(\mathbf{y} \mid \mathbf{x}, \boldsymbol{\theta}) p(\mathbf{x} \mid \boldsymbol{\theta}) p(\boldsymbol{\theta})}{\tilde{p}_{\mathrm{G}}(\mathbf{x}_{-i} \mid x_i, \boldsymbol{\theta}, \mathbf{y})} \right|_{\mathbf{x}_{-i} = \mathbf{x}^*_{-i}(x_i, \boldsymbol{\theta})}.$$

The Gaussian approximation to the full conditional of $\mathbf{x}_{-i} \mid x_i, \boldsymbol{\theta}, \mathbf{y}$ is $\tilde{p}_{\mathrm{G}}(\mathbf{x}_{-i} \mid x_i, \boldsymbol{\theta}, \mathbf{y})$, and $\mathbf{x}^*_{-i}(x_i, \boldsymbol{\theta})$ is the mode. When the full conditional of $\mathbf{x}_{-i} \mid x_i, \boldsymbol{\theta}, \mathbf{y}$ is Gaussian, the approximation need not be done, which is the case in this thesis. This method requires n factorizations of the full precision matrix because $\tilde{p}_{\mathrm{G}}(\mathbf{x}_{-i} \mid x_i, \boldsymbol{\theta}, \mathbf{y})$ needs to be recomputed for each value of x_i and $\boldsymbol{\theta}$. The method is therefore very computationally expensive.

A more computationally efficient method is called the simplified Laplace approximation, which is the default choice in `R-INLA`. This method corrects the Gaussian approximation $\tilde{p}_{\mathrm{G}}(\mathbf{x}_{-i} \mid x_i, \boldsymbol{\theta}, \mathbf{y})$ for skewness and location, and is described more in Rue, Martino and Chopin (2009).

When the approximation $\tilde{p}(x_i, \boldsymbol{\theta} \mid \mathbf{y})$ is found, either by the Laplace or the simplified Laplace approximation, then Equation (3.5) can be integrated numerically with respect to $\boldsymbol{\theta}$ using the sum

$$\tilde{p}(x_i \mid \mathbf{y}) = \sum_k \tilde{p}(x_i, \boldsymbol{\theta}^{(k)} \mid \mathbf{y}) \tilde{p}(\boldsymbol{\theta}^{(k)} \mid \mathbf{y}) \Delta_k.$$

Here $\{\boldsymbol{\theta}^{(k)}\}$ is the set of integration points, which are often in practise the same integration points found in Appendix A.1. The set of weights corresponding to these points is $\{\Delta_k\}$.

APPENDIX B

Estimates of the Parameters for the Spatial Effects

The estimates of the spatial range parameters and marginal standard deviation parameters governing the spatial fields for the two spatial models are shown here with a 95% credible interval. These are the estimates giving the results for the spatial effects shown in Chapter 5.

Estimates of the parameters with a 95% credible interval for the spatial effects for the spatial stationary model is shown in Table B.1. These are the same estimates as shown in Figure 5.9. None of the 95% credible intervals contains zero.

The estimates with a 95% credible interval for the spatial non-stationary model is shown in Table B.2, and also in Figure 5.9. This shows that the 95% credible interval for $\theta_{4,\text{common}}$, $\theta_{2,2018}$, $\theta_{4,2018}$, $\theta_{2,2019}$, and $\theta_{4,2020}$ contains zero. There is thus not evidence that $\tau(s)$ depends on the AADT for the years 2018 and 2019, while there is not evidence that $\kappa(s)$ depends on the AADT for the time constant common field, or the years 2018 and 2020, following from Equation (4.3). For the other parameter estimates the credible interval lays generally far away from zero, indicating that a non-stationarity controlled by the AADT may be reasonable.

Parameter	Mean	95% credible interval
ρ_{common}	731.640	$[572.083, 903.826]$
σ_{common}	0.447	$[0.395, 0.502]$
ρ_{2017}	344.797	$[264.722, 450.819]$
σ_{2017}	0.880	$[0.784, 0.990]$
ρ_{2018}	1377.554	$[952.892, 2084.923]$
σ_{2018}	0.425	$[0.357, 0.493]$
ρ_{2019}	835.061	$[648.379, 1058.180]$
σ_{2019}	1.182	$[1.032, 1.338]$
ρ_{2020}	1574.599	$[1031.969, 2181.938]$
σ_{2020}	0.392	$[0.326, 0.478]$

Table B.1: The posterior parameter estimates for the spatial parameters for the spatial stationary model with a 95% credible interval.

Parameter	Mean	95% credible interval
$\theta_{1,\text{common}}$	9.458	$[8.855, 9.912]$
$\theta_{2,\text{common}}$	-1.304	$[-1.686, -0.805]$
$\theta_{3,\text{common}}$	-5.684	$[-6.012, -5.252]$
$\theta_{4,\text{common}}$	0.252	$[-0.121, 0.543]$
$\theta_{1,2017}$	6.204	$[5.566, 6.731]$
$\theta_{2,2017}$	0.806	$[0.269, 1.430]$
$\theta_{3,2017}$	-4.608	$[-5.003, -4.147]$
$\theta_{4,2017}$	-0.448	$[-0.900, -0.045]$
$\theta_{1,2018}$	9.612	$[8.906, 10.371]$
$\theta_{2,2018}$	-0.554	$[-1.364, 0.158]$
$\theta_{3,2018}$	-5.620	$[-6.155, -5.153]$
$\theta_{4,2018}$	-0.337	$[-0.857, 0.278]$
$\theta_{1,2019}$	7.235	$[6.722, 7.843]$
$\theta_{2,2019}$	-0.279	$[-1.283, 0.555]$
$\theta_{3,2019}$	-5.738	$[-6.205, -5.349]$
$\theta_{4,2019}$	0.800	$[0.214, 1.515]$
$\theta_{1,2020}$	10.136	$[9.473, 10.889]$
$\theta_{2,2020}$	-1.246	$[-2.084, -0.582]$
$\theta_{3,2020}$	-5.542	$[-6.199, -5.025]$
$\theta_{4,2020}$	-0.475	$[-1.091, 0.320]$

Table B.2: The parameter estimates for the spatial parameters for the spatial non-stationary model with a 95% credible interval.

APPENDIX C

Sum-to-Zero Constraints on the Spatial Fields

To ensure that spatial fields does not capture general trends, and from an identifiability viewpoint, sum-to-zero constraints can be used. This was attempted on the spatial fields for the spatial stationary and non-stationary models, as the results in Chapter 5 gave some inconsistent results, especially for the yearly spatial effect for 2019 shown in Figure 5.12c. For this year, the expected rutting is positive for almost all of the road, and the value of the rutting is generally high.

A sum-to-zero constraint was then set on all the spatial fields for the two spatial models. The results for the time constant common field for the spatial stationary model is shown in Figure C.1, while the results for the spatial non-stationary model is shown in Figure C.2. These results are shown with a 95% credible interval, as well as on the map between Bergen and Voss. There are no great discrepancy between these results and those we see in Figure 5.11.

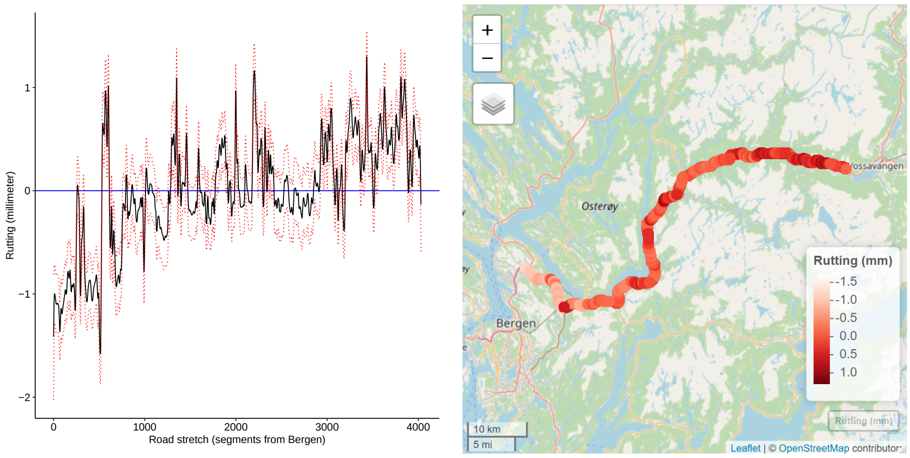

(a) With a 95% credible interval.

(b) On the map.

Figure C.1: The rutting inferred from the common spatial field $\omega_{\mathrm{S}}(s)$ for the stationary model with a 95% credible interval and on the map between Bergen and Voss using sum-to-zero constraints.

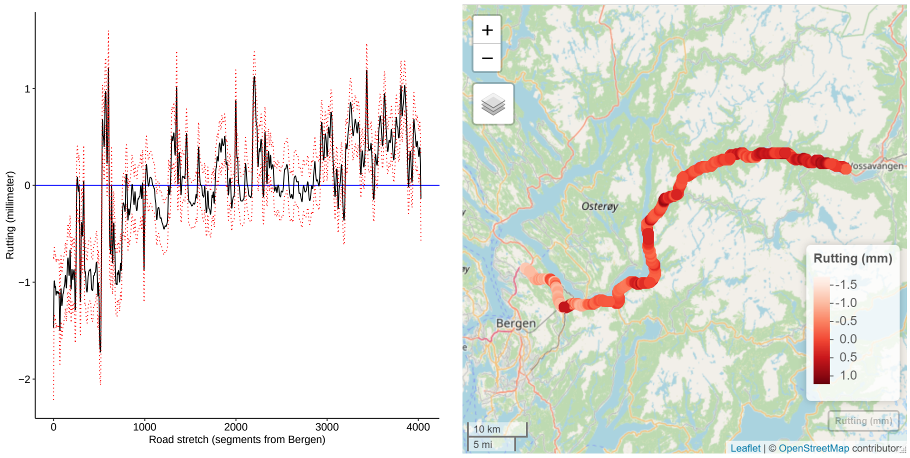

(a) With a 95% credible interval.

(b) On the map.

Figure C.2: The rutting inferred from the common spatial field $\omega_{\text{NS}}(s)$ for the non-stationary model with a 95% credible interval and on the map between Bergen and Voss using sum-to-zero constraints.

The discrepancy of results starts when we look at the results for the yearly varying spatial fields for the spatial stationary model in Figure C.3, and for the spatial non-stationary model in Figure C.4. The results using a sum-to-zero constraint are consistent with the results in Figure 5.12 for the years 2017 and 2018.

The results when using sum-to-zero constraints for the years 2019 and 2020 shows great discrepancies however for both the spatial models. For the year 2019 there is a great spike reaching down to a rutting of about -70 millimeters. In the real data these locations correspond to missing values, so this allows the algorithm to be more liberal in the value it sets after running with the sum-to-zero constraint. This is probably done to compensate for the rest of the rutting being positive, still giving a sum of zero. Similarly, to compensate, the result for the year 2020 has a large positive spike, reaching 10 millimeters of rutting. Because of these discrepancies the sum-to-zero constraint was chosen to not be used.

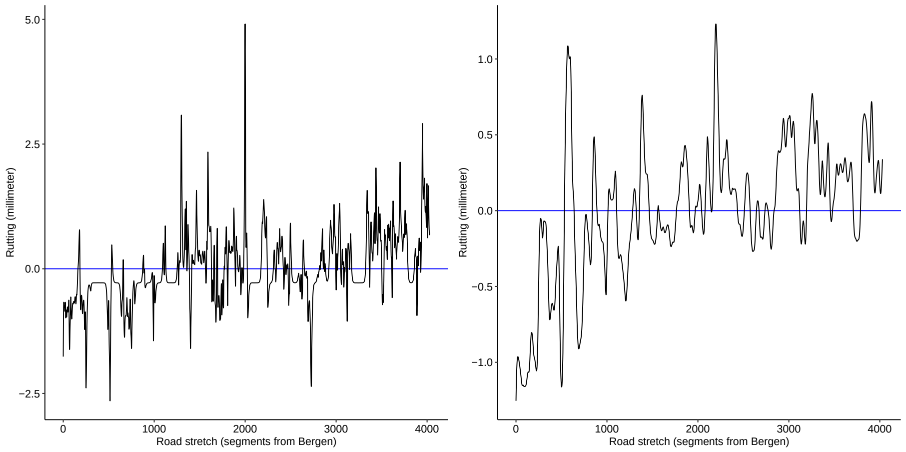

(a) For the year 2017.

(b) For the year 2018.

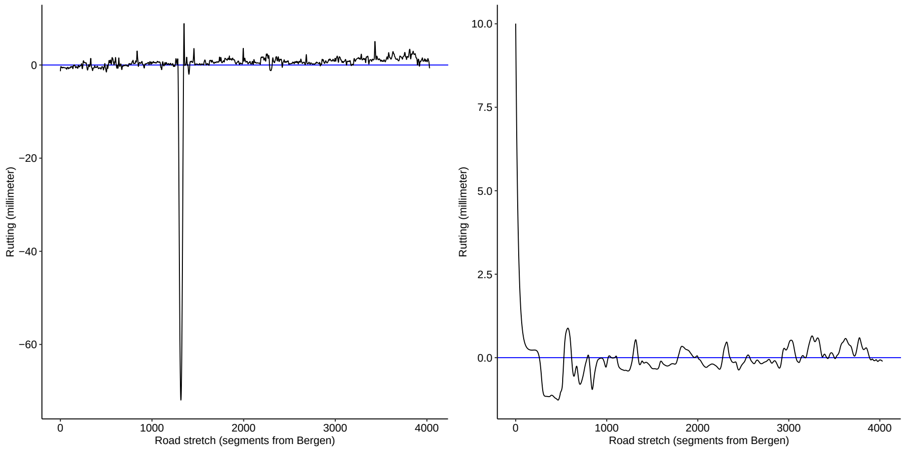

(c) For the year 2019.

(d) For the year 2020.

Figure C.3: The annual spatial deviation from the spatial field $\omega_{\mathrm{S}}(s)$ for each of the years from 2017 to 2020 using sum-to-zero constraints.

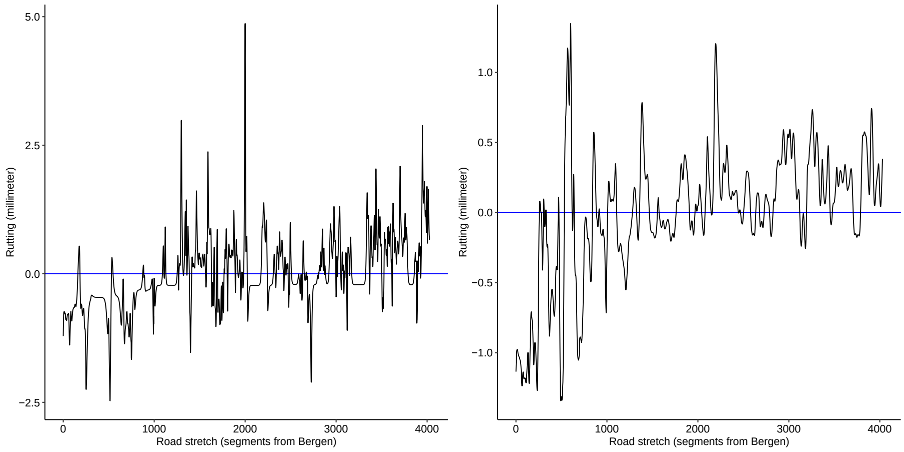

(a) For the year 2017.

(b) For the year 2018.

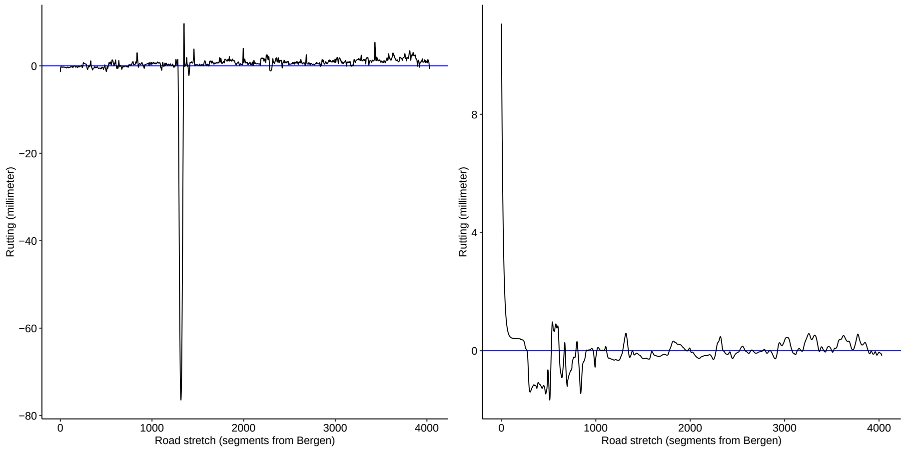

(c) For the year 2019.

(d) For the year 2020.

Figure C.4: The annual spatial deviation from the spatial field $\omega_{\mathrm{NS}}(s)$ for each of the years from 2017 to 2020 using sum-to-zero constraints.

Bibliography

Akaike, H. (1974). ‘A new look at the statistical model identification’. In: *IEEE Transactions on Automatic Control* vol. 19, no. 6, pp. 716–723.

Appelhans, T. et al. (2022). *mapview: Interactive Viewing of Spatial Data in R.* R package version 2.11.0.9000.

Aurstad, J. et al. (2016). ‘The influence of asphalt workmanship on pavement service life’. In: *E&E Congress 2016, 6th Eurasphalt & Eurobitume Congress, Prague, Czech Republic.*

Blangiardo, M. and Cameletti, M. (2015). *Spatial and Spatio-temporal Bayesian Models with R-INLA.* John Wiley & Sons, Ltd.

Brenner, S. C. and Scott, L. R. (2008). *The Mathematical Theory of Finite Element Methods.* Vol. 15. Texts in Applied Mathematics. Springer.

Ebrahimi, B. et al. (2019). ‘Estimation of Norwegian Asphalt Surfacing Lifetimes Using Survival Analysis Coupled with Road Spatial Data’. In: *Journal of Transportation Engineering, Part B: Pavements* vol. 145, no. 3, p. 04019017.

Fuglstad, G.-A. et al. (2017). *Constructing Priors that Penalize the Complexity of Gaussian Random Fields.*

Gelfand, A. et al. (2010). *Handbook of Spatial Statistics.* Chapman & Hall/CRC Handbooks of Modern Statistical Methods. Taylor & Francis.

Gelman, A., Hwang, J. and Vehtari, A. (2014). ‘Understanding predictive information criteria for Bayesian models’. In: *Statistics and Computing* vol. 24, no. 6, pp. 997–1016.

Givens, G. H. and Hoeting, J. A. (2012). *Computational Statistics.* John Wiley & Sons, Ltd. Chap. 1.

Giæver, T. and Johansen, K. (2011). ‘Veileder innsamling og beregning av trafikkdata til støykartlegging’. In: *NPRA Technology report No. 2477.*

Gräler, B., Pebesma, E. and Heuvelink, G. (2016). ‘Spatio-Temporal Interpolation using gstat’. In: *The R Journal* vol. 8 (1), pp. 204–218.

Hubin, A. and Storvik, G. (2016). *Estimating the marginal likelihood with Integrated nested Laplace approximation (INLA).* arXiv: `1611.01450 [stat.CO]`.

Ingebrigtsen, R., Lindgren, F. and Steinsland, I. (2014). ‘Spatial models with explanatory variables in the dependence structure’. In: *Spatial Statistics* vol. 8.

Ingebrigtsen, R., Lindgren, F., Steinsland, I. and Martino, S. (2015). ‘Estimation of a non-stationary model for annual precipitation in southern Norway using replicates of the spatial field’. In: *Spatial Statistics* vol. 14, pp. 338–364.

Krainski, E. T. et al. (2019). *Advanced Spatial Modeling with Stochastic Partial Differential Equations Using R and INLA*. Chapman & Hall/CRC Press.

Lea, J. D. and Harvey, J. T. (2015a). 'A spatial analysis of pavement variability'. In: *International Journal of Pavement Engineering* vol. 16, no. 3, pp. 256–267.

Lea, J. D. and Harvey, J. T. (2015b). 'Using spatial statistics to characterise pavement properties'. In: *International Journal of Pavement Engineering* vol. 16, no. 3, pp. 239–255.

Lindgren, F., Rue, H. and Lindström, J. (2011). 'An explicit link between Gaussian fields and Gaussian Markov random fields: the stochastic partial differential equation approach'. In: *Journal of the Royal Statistical Society: Series B (Statistical Methodology)* vol. 73, no. 4, pp. 423–498.

Lundy, J. R. et al. (1992). 'Wheel Track Rutting Due to Studded Tires'. In: *Transportation Research Record* vol. 1348.

Martino, S. and Riebler, A. (2019). 'Integrated Nested Laplace Approximations (INLA)'. In: *arXiv: Computation.*

Molugaram, K. and Rao, G. S. (2017). 'Chapter 2 - Preliminaries'. In: *Statistical Techniques for Transportation Engineering.* Ed. by Molugaram, K. and Rao, G. S. Butterworth-Heinemann, pp. 25–91.

Moraga, P. (2019). *Geospatial Health Data: Modeling and Visualization with R-INLA and Shiny.* Chapman & Hall/CRC Biostatistics Series.

Myre, J. and Refsdal, G. (2005). 'Pavement Strengthening and Rehabilitation in Norway - Assessing the needs'. In: *Proceedings of the international conferences on the bearing capacity of roads, railways and airfields.*

Norwegian Public Roads Administration (2014). 'Standard for drift og vedlikehold av riksveger'. In: *Håndbok R610.*

Norwegian Public Roads Administration (2020). *Bakgrunn for FoU-programmet SMARTere vedlikehold.* URL: https://www.vegvesen.no/fag/fokusomrader/forskning-innovasjon-og-utvikling/pagaende-programmer-og-prosjekter/smartere-vedlikehold/bakgrunn/ (visited on 04/10/2021).

Norwegian Public Roads Administration (2022a). *Asfalt.* URL: https://www.vegvesen.no/fag/teknologi/vegteknologi/vegbyggingsmaterialer/asfalt/ (visited on 20/02/2022).

Norwegian Public Roads Administration (2022b). *Vegkart.* URL: https://vegkart.atlas.vegvesen.no/ (visited on 22/03/2022).

Norwegian University of Science and Technology (2022a). *Smarter Maintenance of Road Infrastructure (Background).* URL: https://www.ntnu.edu/web/smartermaintenance/about (visited on 23/05/2022).

Norwegian University of Science and Technology (2022b). *Smarter Maintenance of Road Infrastructure (Goals and Focus).* URL: https://www.ntnu.edu/smartermaintenance/goals-and-focus (visited on 23/05/2022).

Olsen, W. S. G. (2021). *Bayesian Models for the Deterioration of Road Covers Based on Annual Rutting Observations.*

Pebesma, E. (2004). 'Multivariable geostatistics in S: the gstat package'. In: *Computers & Geosciences* vol. 30, pp. 683–691.

Pebesma, E. (2018). 'Simple Features for R: Standardized Support for Spatial Vector Data'. In: *The R Journal* vol. 10, no. 1, pp. 439–446.

R Core Team (2020). *R: A Language and Environment for Statistical Computing.* R Foundation for Statistical Computing. Vienna, Austria.

Rue, H. and Held, L. (2005). *Gaussian Markov Random Fields. Theory and Applications*. Chapman and Hall/CRC.

Rue, H., Martino, S. and Chopin, N. (2009). 'Approximate Bayesian inference for latent Gaussian models by using integrated nested Laplace approximations'. In: *Journal of the Royal Statistical Society: Series B (Statistical Methodology)* vol. 71, no. 2, pp. 319–392.

Rue, H., Riebler, A. et al. (2017). 'Bayesian Computing with INLA: A Review'. In: *Annual Review of Statistics and Its Application* vol. 4, no. 1, pp. 395–421.

Saba, R. G. et al. (2006). 'Performance Prediction Models for Flexible Pavements: A State-of-the-art Report'. In: *NPRA Technology report No. 2477*.

Simpson, D. et al. (2017). 'Penalising Model Component Complexity: A Principled, Practical Approach to Constructing Priors'. In: *Statistical Science* vol. 32, no. 1, pp. 1–28.

Sinkhonde, D. and Ngoma, I. (2020). 'Evaluating Flexible Pavement Rutting Damage Caused by Heavy Traffic Loads'. In: *International Journal of Research and Scientific Innovation (IJRSI)* vol. 7, no. 6.

Spiegelhalter, D. J. et al. (2002). 'Bayesian measures of model complexity and fit'. In: *Journal of the Royal Statistical Society: Series B (Statistical Methodology)* vol. 64, no. 4, pp. 583–639.

Sund, E. K. (2012). 'What is the Cost of Eliminating the Maintenance Backlog on National Roads?' In: *NPRA Reports No. 75*.

Sund, E. K. (2013). 'What is the Cost of Eliminating the Maintenance Backlog on County Roads?' In: *NPRA Reports No. 183*.

Svenson, K. et al. (2016). 'Evaluating Needs of Road Maintenance in Sweden with the Mixed Proportional Hazards Model'. In: *Transportation Research Record* vol. 2589, no. 1, pp. 51–58.

Vedvik, E. (2021). 'Spatial non-stationary models for pavement deterioration and traffic accidents'. MA thesis. The Norwegian University of Science and Technology (NTNU).

Watanabe, S. (2010). 'Asymptotic Equivalence of Bayes Cross Validation and Widely Applicable Information Criterion in Singular Learning Theory'. In: *Journal of Machine Learning Research* vol. 11, no. 116, pp. 3571–3594.

Wickham, H. (2016). *ggplot2: Elegant Graphics for Data Analysis*. Springer-Verlag New York.

Yong, L. (2018). *LOO and WAIC as Model Selection Methods for Polytomous Items*.

NTNU
Norwegian University of
Science and Technology